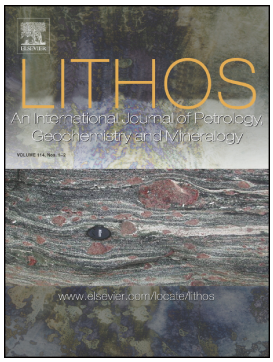

Subduction-related melt refertilisation and alkaline metasomatism in the Eastern Transylvanian Basin lithospheric mantle: Evidence from mineral chemistry and noble gases in fluid inclusions

Barbara Faccini, Andrea Luca Rizzo, Costanza Bonadiman, Theodoros Ntaflos, Ioan Seghedi, Michel Grégoire, Giacomo Ferretti, Massimo Coltorti

PII: S0024-4937(20)30154-7

DOI: https://doi.org/10.1016/j.lithos.2020.105516

Reference: LITHOS 105516

To appear in: *LITHOS*

Received date: 29 May 2019

Revised date: 22 March 2020

Accepted date: 26 March 2020

Please cite this article as: B. Faccini, A.L. Rizzo, C. Bonadiman, et al., Subduction-related melt refertilisation and alkaline metasomatism in the Eastern Transylvanian Basin lithospheric mantle: Evidence from mineral chemistry and noble gases in fluid inclusions, *LITHOS* (2020), https://doi.org/10.1016/j.lithos.2020.105516

Subduction-related melt refertilisation and alkaline metasomatism in the Eastern Transylvanian Basin lithospheric mantle: evidence from mineral chemistry and noble gases in fluid inclusions

Barbara Faccini [a], Andrea Luca Rizzo [a,b], Costanza Bonadiman [a], Theodoros Ntaflos [c], Ioan Seghedi [d], Michel Grégoire [e], Giacomo Ferretti [a], Massimo Coltorti [a,b]

a Dipartimento di Fisica e Scienze della Terra, Università di Ferrara, Italy

b Sezione di Palermo, Istituto Nazionale di Geofisica e Vulcanologia, Palermo, Italy

c Department of Lithospheric Research, University of Vienna, Austria

d Institute of Geodynamics Sabba S. Stefanescu, Romanian Academy, Romania

e GET, CNES-CNRS-IRD-Université Paul Sabatier, OMP, Toulouse, France

Abstract

Calc-alkaline and alkaline magmatic activity is generally separated in space and/or in time. The Eastern Transylvanian Basin in Romania is one of the few places where, during Pleistocene, alkaline eruptions occurred contemporaneously with the calc-alkaline activity. Mantle xenoliths entrained in Perşani Mts. alkaline volcanic products have been studied in order to investigate the interaction of metasomatic agents of different magmatic affinities with the mantle wedge. Based on mineral major and trace element and noble gases in fluid inclusions, two main events have been recognized. The first was a pervasive, complete re-fertilization of a previously depleted mantle by a calc-alkaline subduction-related melt, causing the formation of very fertile, amphibole-bearing lithotypes. This is shown by the a) increased amounts of modal clinopyroxene up to 21.9 % with Al_2O_3 contents up to 8.16 wt%, higher than what is expected for clinopyroxene in Primordial Mantle; b) $^4He/^{40}Ar^*$ ratios up to 1.2, within the reported range for mantle production; c) $^3He/^4He$ in olivine, opx and cpx of 5.8±0.2 Ra, among the most radiogenic values of European mantle, below the typical MORB mantle value (8±1 Ra), reflecting recycling of crustal material in the local

lithosphere. The second event is related to later interaction with an alkaline metasomatic agent similar to the host basalts that caused slight LREE enrichment in pyroxenes and disseminated amphiboles and precipitation of vein amphiboles with a composition similar to amphiboles megacrysts also found in the Perşani Mts. volcanic deposits. This is highlighted by the $^{4}He/^{40}Ar^{*}$ and $^{3}He/^{4}He$ values found in some opx and cpx, up to 2.5 and 6.6 Ra, respectively, more typical of magmatic fluids.

Keywords: MANTLE REFERTILISATION, EASTERN TRANSYLVANIAN BASIN, NOBLE GASES, POST-COLLISIONAL, SUBDUCTION-RELATED METASOMATISM

1. INTRODUCTION

Xenoliths representing mantle wedge fragments as defined by Arai and Ishimaru (2008) are rarely found in post-collisional, subduction-related geodynamic settings. They have been collected mainly in arc volcanics of the western Pacific and have allowed reconstruction of dynamics and metasomatic processes occurring in the mantle wedge of large, mature subduction zones (Yoshikawa et al., 2016; Bénard et al., 2018). Mantle wedge xenoliths are rarer in eastern Pacific and Atlantic subduction systems (e.g. Brandon and Draper, 1996; Parkinson et al., 2003; Faccini et al., 2013). In Europe, the tectonic complexity and peculiar characteristics of the recent subduction zones (Edward and Grasemann, 2009), as well as the presence of ultramafic xenoliths only in alkaline volcanic products, makes it more difficult to establish if they come from a subduction context and can thus be representative of the mantle wedge. In some cases, however, a subduction-related metasomatism has been recognized both from mineral (Coltorti et al., 2007a; Bianchini et al., 2011) and fluid inclusion compositions (Martelli et al., 2011; Créon et al., 2017).

The Carpathian-Pannonian is one of the most promising areas for the investigation of subduction influence on the local magma sources. Its evolution has been "an interplay of subduction and diapiric uprise in the mantle" (Konečný et al., 2002) where landlocked oceanic lithosphere sections foundered (Edward and Grasemann 2009), causing subduction zone arching and retreat via slab roll-back and consequent asthenosphere doming and corner flow. It comprises several districts (Styria Basin and Burgenland, Little and Great Hungarian Plains and Transylvanian Basin), whose complex evolution from the Neogene to the Quaternary saw the systematic eruption of alkaline and ultrapotassic magmas after the main phases of calc-alkaline volcanic activity (Seghedi and Downes, 2011) within variable time spans (1-10 Ma, Pécskay et al., 2006). This would imply major changes in the magma source that should be reflected in the textural-chemical-petrological characteristics of the upper mantle. Among all xenolith occurrences in the Pannonian Basin those entrained in the Na-alkaline lavas of the Perşani Mts. in the Eastern Transylvanian Basin, erupted very close to the youngest calc-alkaline volcanic fields linked to the post-collisional stage along the Carpathian Bend (Seghedi et al., 2011, 2019), are the most promising candidates for representing the mantle wedge of a Carpathian-Pannonian-type subduction zone.

In this paper, we present the results of the petrography, mineral chemistry and noble gases study of a new suite of mantle xenoliths from Perşani Mts. In addition to the "classical" petrological approach, noble gases in fluid inclusions add complementary information for evaluating the degree of partial melting of the local mantle, as well as for revealing the origin of metasomatic fluids and the occurrence of a refertilization process that modified the original mantle features (e.g., Rizzo et al., 2018).These tracers helped revealing the presence of two different kinds of metasomatism: one related to the injection of alkaline melts similar to the host magma and another defined as a pervasive refertilisation of the mantle domain by calc-alkaline subduction-related melts. Both types of metasomatism are intimately linked to the major geodynamic changes which occurred in the area.

2. GEOLOGICAL SETTING

The Pliocene–Quaternary Perșani Mountains Volcanic Field (PMVF) is located in the internal part of the Carpathian Bend area, in the south-eastern corner of the Transylvanian Basin (Fig. 1). It is the youngest and largest monogenetic volcanic field in south-eastern Europe. This volcanism was coeval with the last peak of crustal deformation in the Carpathian Bend (Merten et al., 2010) as well as with the orogenic adakite-like calc-alkaline and K-alkaline volcanism of the southernmost Harghita Mountains, located 40 km to the east (Szakács et al., 1993; Seghedi et al., 2004). The PMVF is underlain by a relatively thick continental crust (35–40 km), whereas the whole lithosphere is relatively thin (60–80 km; Martin et al., 2006; Seghedi et al., 2011).

The volcanic activity occurred between 1.2 Ma and 0.8 Ma, generating numerous monogenetic volcanic centers in a 22 km long and 8 km wide area (Seghedi et al., 2016). The occurrence of three contemporaneous magma sources (Na-, K-alkaline, and adakite-like calc-alkaline) in a narrow area has been facilitated by the same regional tectonic event, coeval with the last episode (latest Pliocene onward) of tectonic inversion in the Southeastern Carpathians, linked to indentation of the Adria micro-plate (Matenco et al., 2007).

The petrological features of the PMVF basalts are similar to those of continental intraplate alkali basalts worldwide (e.g., Lustrino and Wilson, 2007; Harangi et al., 2014), with some subtle differences suggesting an influence by subduction components. The frequent occurrence of mantle xenoliths in the PMVF provides evidence for rapid magma ascent (Harangi et al., 2013).

3. PETROGRAPHIC OUTLINE

3.1 Sample location and classification

PMVF mantle xenoliths were collected from pyroclastic deposits of La Gruiu and Fântana eruptive centers and from lava flows along the Bârc and Trestia creeks (Fig. 1). The xenoliths are fresh, with sizes varying from 4 to 12 cm in diameter. Modal estimates were obtained mainly by thin-section

point counting; if the samples were large enough to allow whole rock analyses, the point counting results were crosschecked with mass balance calculations between whole rock and mineral major element compositions.

Lherzolite is the most common rock type, with a total of 30 out of 34 samples (ESM0). The main characteristic is the almost ubiquitous presence of disseminated pargasitic amphibole, texturally equilibrated with the other constituent minerals and whose modal abundance varies between traces and 11.5 %. Lherzolite LAG52 displays a 1 mm-thick amphibole vein, as well as disseminated amphibole and TRE4 is a composite amphibole-bearing lherzolite/websterite (respectively referred as TRE4 Pd and TRE4 Px).

Detailed observations of microstructures and olivine Crystal Preferred Orientation carried out by Falus et al. (2011) showed that PMVF xenoliths record deformation by dislocation creep under different ranges of temperature, stress and strain rate conditions. This resulted in a continuous textural gradation from coarse-grained to fine-grained mylonitic types, the latter making up about 15% of the ultramafic rocks. Such a textural transition is evident in our suite, although only one sample is clearly mylonitic. Coarse to medium-grained samples are predominant and can be satisfactorily described on the basis of the petrographic classification of Mercier and Nicolas (1975). Following these considerations, PMVF lherzolites were divided into two main textural groups: Protogranular and Porphyroclastic (Table 1), whose detailed petrographic description is provided in ESM0.

3.2 Protogranular group

This group can be further divided into two sub-groups, on the basis of specific textural features: *Protogranular s.s. (Pr s.s.)* and *Protogranular with small, rounded grains (Pr srg)* (Table 1; ESM0). Both sub-groups correspond to the coarse-grained peridotites described by Falus et al. (2011) who, however, defined them as being porphyroclastic, showing such a continuous variation in grain size that the distinction between porphyroclasts and recrystallized grains has been hindered.

These kinds of texture would form at high-temperature (as also noted by Chalot-Prat and Boullier, 1997), low-stress conditions like those prevailing at deep levels within the lithosphere and at the lithosphere/asthenosphere boundary. We decided to classify them as Protogranular on the basis of their close resemblance to the Mercier and Nicolas (1975) type description, being aware of the fact that no "pristine" un-deformed lithospheric mantle portions are probably preserved anywhere on Earth and all textural types actually are the result of a series of deformation and recrystallization events.

3.3 Porphyroclastic group

This group is divided into two sub-groups: *Porphyroclastic with large, rounded grains (Po lrg)* and *Porphyroclastic s.s. (Po s.s.).* (Table 1; ESM0). They correspond to intermediate to fine-grained porphyroclastic peridotites described by Falus et al. (2011). This texture would indicate lower temperatures (Chalot-Prat and Boullier, 1997) and higher stress conditions with respect to the Protogranular group, suggesting that these samples may come from shallower depth, probably the upper levels of the lithospheric mantle.

3.4 Description of the fluid inclusions

Irrespective of textural type, fluid inclusions (FI) are scarce in PMVF mantle xenoliths and very small (only few μm across). As described by Rizzo et al., 2018 and according to the classification of Roedder (1984), FI occur i) as primary inclusions, generally isolated or arranged in short, tiny trails and/or ii) as secondary inclusions, often forming cluster stripes or trails along planes. In PMVF xenoliths, primary FI could not be clearly identified; the few observed FI are secondary inclusions.

4. ANALYTICAL METHODS

Mineral major elements. In situ mineral major element compositions were determined using a CAMECA SX100 electron microprobe, at the Department of Lithospheric Research, University of Vienna. Operating conditions were: 15 kV accelerating voltage, 20 nA beam current, 20 s counting time on peak position. Natural and synthetic standards were used for calibration and PAP corrections were applied to the intensity data (Pouchou and Pichoir, 1991).

Mineral trace elements. In situ trace element concentrations in pyroxenes and amphiboles were obtained by Laser Ablation Microprobe Inductively Coupled Plasma Mass Spectrometry (LAM-ICP-MS) at the IGG - C.N.R., Pavia (Italy). A 40–80 μm beam diameter was used, depending on mineral phase. NIST 610 and NIST 612 standard glasses were used to calibrate relative element sensitivity; precision and accuracy were assessed by standard sample BCR-2. Each analysis was corrected with internal standards, using CaO for clinopyroxene and amphibole and SiO_2 for orthopyroxene. On the whole, the theoretical detection limit ranges from 10 to 20 ppb for REE, Ba, Th, U and Zr and 2 ppm for Ti.

Noble gases measurements. Eleven aliquots of pure, unaltered olivine, orthopyroxene and clinopyroxene larger than 0.5 mm were handpicked for noble gases analyses (He, Ne, Ar) in FI from the same set of samples selected for the mineral chemistry analyses (LAG1, LAG2, LAG21, LAG24, LAG51, LAG52, PAR04, TRE1, TRE2, TRE3, TRE4). The crystals were prepared and analyzed at the Istituto Nazionale di Geofisica e Vulcanologia (INGV), Sezione di Palermo (Italy), following the local isotope laboratory protocol reported by Rizzo et al. (2018).

The element and isotope composition of noble gases (He, Ne, and Ar) was determined by loading the mineral aliquots into a six-position stainless-steel crusher. FI were released by in-vacuo single-step crushing at about 200 bar. He isotopes (^{3}He and ^{4}He) and Ne isotopes (^{20}Ne, ^{21}Ne, and ^{22}Ne) were measured using two different split-flight-tube mass spectrometers (Helix SFT, Thermo Scientific). Ar isotopes (^{36}Ar, ^{38}Ar, and ^{40}Ar) were simultaneously analyzed by a multicollector mass spectrometer (Argus, GVI).

The analytical uncertainty of $^{40}Ar/^{36}Ar$ (1 σ) was <2.4%, while those of $^{20}Ne/^{22}Ne$ and $^{21}Ne/^{22}Ne$ were <4% and <4.3%, respectively (with the exception of one measurement in opx from LAG1 that was 20.3% for $^{21}Ne/^{22}Ne$). The analytical uncertainty of the $^{3}He/^{4}He$ (1 σ) was between 0.7 and 12%.

Full description of analytical methods and data correction is reported in ESM1.

5. WHOLE ROCK AND MINERAL CHEMISTRY

5.1 Whole rock

Whole rock compositions (ESM2-1) were determined for 15 samples, representative of all the recognized textural tpes. Xenoliths belonging to the Protogranular group (*Pr s.s.* and *Pr srg*) have lower MgO and higher SiO_2, TiO_2, Al_2O_3 and CaO than those belonging to the Porphyroclastic group (*Po s.s.* and *Po lrg*. Na_2O and FeOtot are similar in both Groups.

Ni, Cr and Co contents are very similar for all textural types while Zr and V tend to be lower in Porphyroclastic than in Protogranular group. No difference was envisaged between amphibole-bearing and anhydrous samples, although the latter are too scarce to be statistically representative.

5.2 Mineral major elements

Description of major element composition includes primary phases only, as glass vein and patches where small secondary phases have been found are rare and volumetrically negligible.

5.2.1 Olivine

Irrespective of the textural group, olivine has forsteritic component (Fo) ranging from 88.9 to 91.8 (Table 1; ESM2-2), the lowest values belonging to grains close to the amphibole vein of lherzolite LAG52, while the highest being recorded in the large porphyroclasts of anhydrous harzburgite

TRE1. NiO varies from 0.34 to 0.43 wt% and has no correlation with Fo nor with textural group. According to Herzberg et al. (2016), such high NiO is typical of depleted lithologies.

5.2.2 Clinopyroxene

Clinopyroxene (cpx) exhibit a large range of mg# (89.0 - 92.9) and Al_2O_3 (3.27 -8.16 wt%) (Fig. 2A; ESM2-2). Cpx of *Pr s.s.*, *Pr srg* and *Po lrg* sub-groups are more fertile than those in *Po s.s* sub-group, in agreement with Szabó et al. (1995a), who also noticed higher basaltic components in the less deformed xenoliths. Cpx in TRE4 Px have lower mg# and higher Al_2O_3 than cpx in TRE4 Pd (Fig. 2A). TiO_2 is always lower than 0.71 wt%, with the lowest values found in cpx of anhydrous harzburgite TRE1 (Fig. 2B). As already noticed by Falus et al. (2008), a positive correlation between Al_2O_3 and Na_2O is observed, with *Po s.s.* and *Pr s.s.* falling respectively at the lowest and highest ends of the trend (Fig. 2C).

5.2.3 Orthopyroxene

Orthopyroxene (opx) have mg# varying from 89.1 to 92.1(Fig. 3A, ESM2-2). Analogously to olivine, the lower values characterize opx close to the amphibole vein in LAG52 while the highest values are recorded by anhydrous harzburgite TRE1. TRE1 opx also have the lowest Al_2O_3 contents (2.84 – 3.62 wt%) of the entire PMVF xenolith suite (2.84 – 5.90 wt%). No remarkable major element compositional difference could be observed between porphyroclasts and neoblasts. However, in contrast with Szabó et al. (1995a), Vaselli et al. (1995) and Falus et al. (2008), there is a slight difference in geochemical composition coupled with textural variations. Ca discriminate between the textural groups, with higher CaO in Protogranular than in Porphyroclastic types (Fig. 3B).

5.2.4 Amphibole

Disseminated amphiboles are the dominant textural type in the PMVF mantle xenoliths. The only vein found (LAG52) resembles those already described in the literature (Vaselli et al., 1995; Zanetti et al., 1995).

Disseminated amphibole mg# spans from 86.8 (LAG52) to 89.5 (TRE2) (Fig. 4A; ESM2-2); amphibole from *Pr s.s.*, *Pr srg* and *Po lrg* are rather constant in composition within the same sample, with Al_2O_3 contents in the narrow range of 15.3 - 16.3 wt%, while those of the composite sample TRE4 (*Po s.s.*) go from 14.6 to 16.2 wt%, the higher variability being from TRE4 Px. On the whole, Al_2O_3 contents are among the highest for calcic amphibole in European mantle xenoliths and, more broadly, in mantle xenoliths occurring in both intraplate and suprasubduction geodynamic settings, at comparable mg# (ESM3-1). CaO in amphiboles of *Pr s.s.*, *Pr srg* and *Po lrg* textural sub-groups is lower than those of the *Po s.s.* sub-group.

The amphibole vein of LAG52 has the lowest mg# and the highest K_2O. Its Na_2O, Al_2O_3 and Cr_2O_3 are lower and TiO_2 is higher (Fig. 4B) with respect to disseminated amphibole in the same sample. A continuous variation occurs between LAG52 vein amphibole, the veins analyzed by Vaselli et al. (1995) and PMVF pargasitic to kaersutitic amphibole megacrysts (Downes et al., 1995; Zanetti et al., 1995; Demény et al., 2005) (Fig. 4B).

5.2.5 Spinel

Primary spinel are Al-rich (Table1; ESM2-2), with very low cr# (6.64 - 16.0) but high mg# (74.8 – 79.19), comparable to that of abyssal peridotite spinel (Seyler et al., 2003; Schmädicke et al., 2011). Al-rich spinel associated to LAG52 vein amphiboles are also relatively iron-rich (mg# 70.6 – 71.4), whereas primary spinel of the anhydrous harzburgite TRE1 are clearly distinct, having comparable mg# (71.8-74.6) but the highest cr# (28.6-34.6) values of the entire xenolith population (Fig. 5). In the Olivine-Spinel Mantle Array (OSMA, ESM3-2), all spinel fall in the lower end of the continental peridotites field, with the exception of TRE1.

5.3 Mineral trace elements

Pyroxenes and amphibole were measured with an average of 5 spots *per* sample. If the trace element content of a phase was very homogeneous, the mean concentration of each element was calculated: this reduced dataset was used for modeling. On the basis of chondrite-normalized REE patterns, pyroxenes and amphibole have been divided into three Groups.

5.3.1 Clinopyroxenes

Cpx (Table 2; ESM2-3) in individual sample correspond to a single Group, with exception of BARQ4 and TRE4 that have cpx belonging to two Groups.

Group 1 (BARQ4, LAG21, LAG24 and TRE4 Pd) displays slightly Light Rare Earth Element (LREE) to Middle (MREE) convex-upward depleted patterns (Fig. 6A), with $(La/Yb)_N$ spanning from 0.34 to 0.50. In this Group, Heavy Rare Earth Element (HREE) contents are slightly variable, with $(Yb)_N$ ranging from 9.02 to 16.1. In Chondrite-normalized trace element diagrams (Fig. 6B), they show variable degrees of enrichment in Th and U (up to 12.2 and 37.5, respectively) and a ubiquitous negative Ti anomaly; Zr and Hf can be decoupled.

Group 2 samples (BARQ4, LAG1, TRE2 and TRE4 Px), have a similar REE profile to Group 1 but with a flatter M to HREE pattern, highly variable HREE contents [$(Yb)_N$, 5.76 – 16.4)] and slight enrichments in La and Ce [$(La/Yb)_N$ = 0.38 - 0.89)] (Fig. 6C). In Chondrite-normalized trace element patterns, Group 2 cpx are similar to those of Group 1 but for a slight positive Sr anomaly (Fig. 6D).

Group 3 (LAG51, LAG52 and TRE1) is the most LREE-enriched (Fig. 6E), with the highest $(La/Yb)_N$ ratios of the whole suite (1.01 – 5.45) and spoon-shaped REE patterns. These cpx also have the highest Th and U contents, up to 48 and 102 x Chondrite, respectively (Fig. 6F). HREE are similar to those of the other Groups [$(Yb)_N$, 5.88 – 18.7]. Group 3 includes cpx of anhydrous harzburgite TRE1, showing the same REE profile with the lowest M-HREE contents.

There is no neat correspondence between the types recognized from texture and major elements and cpx Groups according to their trace element inventory. Cpx modal content increases in the sequence Group 3 - Group 1 – Group 2 (Table 1).

5.3.2 Orthopyroxenes

Opx (Table 3; ESM2-3) Chondrite-normalized trace element patterns are characterized by steep REE patterns and positive Zr-Hf and Ti anomalies (Fig. 7).

Opx associated with Group 1 cpx are the most depleted (beside a slight La enrichment) (Fig. 7A), with negative to positive Sr anomaly {Sr*= Sr/[(Sm+Nd)/2], 0.07 – 2.43} and low Th contents (up to 0.56 x Chondrite) (Fig. 7B).

Group 2 opx show LREE enrichment in agreement with those of the associated cpx (Fig. 7C); they largely overlap opx of Group 1, with higher Th (up to 3.12 x Chondrite) and a ubiquitous negative Sr anomaly (Sr*, 0.15 – 0.89) (Fig. 7D).

Opx associated with Group 3 cpx show an overall La to Tb enrichment (Fig. 7E) and the highest Th contents (up to 7.77 x Chondrite) but have similar Sr* to that of Group 1 opx (0.02 – 1.45) (Fig. 7F).

5.3.3 Amphiboles

Chondrite-normalized trace element and REE patterns of disseminated amphibole (Table 4; ESM2-3) closely mimic those of the coexisting cpx (Fig. 8) in each sample and, on average, for each Group.

Group 1 amphiboles have the most depleted [$(La/Yb)_N$, 0.30 – 0.54], well-defined convex upward REE patterns (Fig. 8A); they show either positive or negative Nb-Ta anomalies (Fig. 8B) even though their contents are low (up to 3.04 ppm Nb; up to 0.21 ppm Ta). Positive Nb-Ta anomalies are always associated with negative Th-U anomalies and *vice versa*, thus the higher Th and U

values (up to 5.95 and 16.9 x Chondrite, respectively) are reached in amphiboles with the lowest Nb contents. Group 1 has also a pronounced positive Ti anomalies (Ti* = Ti/[(Eu+Gd)/2], 0.83 – 2.28). Group 2 includes amphiboles showing slight La and Ce enrichment [$(La/Yb)_N$, 0.33 – 1.30] and less convex REE pattern with respect to Group 1 (Fig. 8C). The opposite behavior between Nb-Ta and Th-U anomalies persists (Fig. 8D), with similar Nb and Ta contents (up to 5.62 ppm Nb; 0.28 ppm Ta, respectively) and Th spikes (up to 13.6 x Chondrite). The negative Ti anomaly is similar (Ti*, 0.78 – 2.99).

Amphiboles in Group 3 are strongly enriched in LREE [$(La/Yb)_N$, 1.27 – 3.75] with respect to the previous Groups, forming smooth spoon-shaped patterns (Fig. 8E). They have Th and U values slightly higher than those of the other groups (up to 18.2 and 22.1, respectively) and reach the highest Nb contents (67.4 x Chondrite) among disseminated amphiboles (Fig. 8F).

The vein amphibole (LAG52) are incorporated in Group 3 as a single average (Fig. 8E, F). They display a strongly fractionated REE pattern with L-MREE enrichments [$(La/Yb)_N$, 3.46 - 5.90], the highest HFSE contents [$(Nb)_N$, 257 x Chondrite; $(Zr)_N$, 24 x Chondrite; $(Hf)_N$, 28.4 x Chondrite] and weak negative Ti anomalies (Ti*, 0.69 – 1.40). Their patterns fit well those of amphibole veins described by Zanetti et al. (1995), Vaselli et al. (1995) and Chalot-Prat and Bouillier (1997) (ESM3-3). The trace element budget of these veins shows many similarities with amphibole megacrysts (ESM3-3, Zanetti et al., 1995, Downes et al., 1995) which, however, are on average characterized by slightly lower LREE and a strongly positive Ti anomaly (Ti*, 1.71 – 4.08).

5.4 Noble gas elemental and isotopic compositions

Olivine systematically shows the lowest concentration of ^4He and $^{40}Ar^*$ (where the star indicates that ^{40}Ar was corrected for air contamination; see, ESM1 for details on the used equation), while cpx and opx have a similar range of values (ESM3-4). The highest concentration for the three minerals is found in LAG52 that also shows the lowest mg#. ^4He is positively correlated with $^{40}Ar^*$, indicating that ^4He-rich FI are also $^{40}Ar^*$-rich and, probably, rich in the other gas species.

The $^{4}He/^{20}Ne$ ratio is 0.7-41.7 in ol, 11–1960 in opx, and 8.3–1394 in cpx (Table 5). The $^{40}Ar/^{36}Ar$ ratio is 286–326 in ol, 350–879 in opx, and 319–1867 in cpx (Table 5). The $^{20}Ne/^{22}Ne$ and $^{21}Ne/^{22}Ne$ ratios are 9.8–10.0 and 0.0283–0.0327, respectively, in olivine, 9.8–10.1 and 0.0291–0.0342 in opx, and 9.9–10.1 and 0.0290–0.346 in cpx (Table 5 and Fig. 9).

The $^{3}He/^{4}He$ ratio corrected for air contamination (Rc/Ra value) is 1.5–5.9 Ra in olivine, 5.4–6.8 Ra in opx, and 2.2–6.8 Ra in cpx (Table 5 and Fig. 10). The highest $^{3}He/^{4}He$ values within olivine were measured in LAG52 and TRE2 (5.4 and 5.9 Ra, respectively), and only in the case of LAG52 it corresponds to the highest concentration of ^{4}He (94×10^{-14} mol/g) and $^{40}Ar^{*}$ (42×10^{-14} mol/g) (Fig. 10). At progressively lower concentration of ^{4}He and $^{40}Ar^{*}$, $^{3}He/^{4}He$ values decrease. The highest $^{3}He/^{4}He$ ratios in opx and cpx are measured in TRE1 and TRE2 (Fig. 10; Table 5).

6 DISCUSSION

6.1 Mineral equilibrium and temperature estimation

The Mg and Fe equilibrium exchange (Brey and Köhler, 1990) among peridotite minerals allows evaluation of the extent to which mineral pairs are in equilibrium, coherently with their Fe/Mg distribution. Irrespective of textural type and amphibole modal percentage, the Fe/Mg exchange between olivine and opx of PMVF samples reproduces, within the experimental error, the slope of olivine-opx lines calculated for temperatures varying between 927 and 727 °C (1300 - 1100 °K) in the pressure range of 1.5 - 2.0 GPa. Olivine-cpx and opx-cpx pairs, distinguished by textural types, also reflect ideal Fe/Mg equilibrium (Brey and Köhler, 1990) in the same temperature and pressure ranges. Minerals in close proximity to host basalt veinlets, showing destabilization due to local thermal effects, were discarded. Equilibrium between olivine and spinel was also evaluated, using the same method described in Faccini et al. (2013). Taking into account the diffusion corrections (Lehmann, 1983), Fe-Mg distribution coefficient between olivine and Al-spinel is estimated in the range of 0.90 - 1.23 (Jamieson and Roeder, 1984) at T= 1000-1200 °C. The abundance of

disseminated amphibole in PMVF peridotites (Table 1; ESM0) cannot be ignored in discussing the potential intra-mineral equilibrium conditions. Experimentally-determined average Fe-Mg distribution coefficient ($Kd_{Fe\text{-}Mg}^{cpx\text{-}amph}$) between cpx and amphibole in basanite melts is 0.76 $\pm$ 0.21 (Pilet et al., 2010). This value is also constrained by Ca contents and the subsolidus equilibrium between the two minerals is resolved with [Ca/(Ca+Mg+Fetot)] ~ 1.6 (Forshaw et al. 2019), a condition fully satisfied by amphibole/cpx pairs in PMVF peridotitic xenoliths.

In the light of these findings, temperature estimations have been carried out using the two pyroxene equations of Brey and Köhler (1990) and Taylor (1998) (Table 1). Brey and Köhler (1990) geothermometer yielded temperatures from 778 to 1056 °C at 2.0 GPa. Taylor (1998) formula gave similar results (793-1009 °C at 2.0 GPa), with differences between the two methods always less than 60°C. Only TRE4 Px has a temperature lower than 800 °C. *Po s.s.* recorded, on average, lower temperatures than the other three textural sub-groups. The *Po lrg* group is intermediate between the Protogranular group and *Po s.s*, suggesting a decrease in temperature at increasing degree of deformation in PMVF samples, in agreement with the results of Falus et al. (2008) and what has been observed for other mantle xenolith suites from the Pannonian Basin (Embey-Isztin et al., 2001; Ntaflos et al., 2017).

6.2 Oxygen fugacity and pressure conditions

Assuming that thermodynamic parameters are known and activity/composition relations can be assessed, oxygen fugacity (fO_2) in mantle peridotites may be calculated from the heterogeneous redox equilibria:

Fayalite (olivine) + O_2 (fluid) = Ferrosilite (opx) + Magnetite (spinel).

The calculation is hampered by uncertainties in the activity/composition relations of magnetite component in spinel (Wood and Virgo, 1989). Since magnetite solid solution is low in mantle spinel ($\leq$ 2.5% in this xenolith population), typical analytical errors translate into considerable fO_2 uncertainties. We applied the semi-empirical equation of Ballhaus et al. (1991), using the magnetite

composition/activity model of Wood and Virgo (1989). The fO_2 calculated in terms of divergence from the fayalite-magnetite-quartz (FMQ) buffer are in the restricted range of - 0.19 to - 1.78, with the lowest values belonging to the *Po s.s.* anhydrous harzburgite TRE1 (Table 1; ESM3-5). These values are comparable to those typical for both off-craton Sub-Continental Lithospheric Mantle (SCLM) and supra-subduction zones (Foley, 2011; Bénard et al., 2018) and to those calculated for Pannonian Basin mantle xenoliths by Szabó et al. (1995b). A weak (R^2 = 0.4) positive correlation between fO_2 and the modal percentage of the redox sensitive phase amphibole have been observed, in agreement with the result of Sorbadere et al. (2018).

The pressure of amphibole formation could be tentatively estimated. Mandler and Grove (2016) established that alkali content of amphibole in the Earth's mantle is a linear function of pressure and temperature and less dependent on bulk compositional variations and water contents, allowing formulation of an empirical thermobarometer for pargasite-bearing garnet (and spinel) peridotites. To avoid circular reference, we introduced in eq. 1 of Mandler and Grove (2016) the temperatures calculated from Brey and Köhler (1990) geothermometer. According to the Mandler and Grove (2016) equation, PMVF amphibole-bearing lherzolites equilibrated between 2.5 and 2.7 GPa (Table 1), which seem to be rather high pressures as no garnet is present in their mineral assemblage. These rocks have bulk Cr_2O_3/Al_2O_3 ratios (0.09-0.14) comparable to the experimental fertile hydrous (H_2O= 0.65 wt%) lherzolite (0.10), in which the spinel–garnet transition occurs below 2.5 GPa. Taking into account the error and the different water content between natural and experimental lherzolites, the pressure prediction for PMVF amphibole equilibration are therefore consistent with these samples having last equilibrated in the upper pressure limit of the spinel stability field (Ziberna et al. 2013). Consequently, a rather deep origin of the PMVF mantle xenoliths cannot be discounted. The opx-cpx-spinel clusters found within some samples could be symptomatic of former garnet as suggested by Falus et al. (2000), who hypothesized a mantle domain moving from a garnet-bearing region at pressures higher than 3.0 GPa to a shallower level (1.9 - 2.1 GPa), inferring an upwelling of the PMVF mantle section of 40-60 km. This occurred in

the frame of a highly arcuate subduction zone, where rapid tectonic changes were strictly correlated with accelerated slab steepening (Edward and Grasemann, 2009), asthenosphere uprise (Kovács et al., 2018) in a post-collisional stage and regional stress redistribution (Seghedi et al., 2011).

6.3 Processes that modify the geochemistry of FI

6.3.1 Atmospheric contamination

The isotope composition of Ne and Ar, and complementarily the $^{4}He/^{20}Ne$ ratio in FI of PMVF xenoliths highlights a variable air contamination (Figs. 9 and 11, Table 5), which progressively decreases from olivine to cpx, probably due to the increasing concentration of He-Ne-Ar trapped in FI of the pyroxenes. This is clearly shown by the three Ne isotopes plot (Fig. 9), in which our data fall along or slightly below the theoretical mixing line between air and a MORB-like mantle, defined by Sarda et al. (1988) and Moreira et al. (1998) at $^{21}Ne/^{22}Ne = 0.06$ and $^{20}Ne/^{22}Ne = 12.5$. A similar indication comes from the $^{40}Ar/^{36}Ar$ and $^{3}He/^{36}Ar$ values (Fig. 11), which are well below the theoretical ratio in the mantle ($^{40}Ar/^{36}Ar$ up to 44,000 and $^{3}He/^{36}Ar$~0.45; e.g., Moreira et al., 1998; Ballentine et al., 2005), and fall along the binary mixing between air and a MORB-like mantle. Air in FI from mantle xenoliths could be linked to a direct contamination in the SCLM (e.g. Rizzo et al. 2018). Further details on this topic are reported in ESM4.

6.3.2 Diffusive fractionation

Comparing ^{4}He and $^{40}Ar^{*}$ with $^{3}He/^{4}He$ (Fig. 10) we notice that, at concentrations of ^{4}He and $^{40}Ar^{*}$ below ~1.0-2.0×10^{-13} mol/g, $^{3}He/^{4}He$ values decrease. This behaviour mostly regards olivine and cpx from sample TRE4. These differences may have originated from preferential diffusive loss of ^{4}He and $^{40}Ar^{*}$ (e.g., Burnard et al., 1998; Burnard, 2004; Yamamoto et al., 2009), as explained in ESM4.

6.4 Melting and refertilisation events

Whole rock and modal compositions of PMVF mantle xenoliths have been compared to melting models for off-craton peridotites, in order to understand the melting history of the sampled lithospheric section. The samples align with the depletion model trends of Niu et al. (1997), although a tendency towards lower modal olivine and higher cpx can be seen (ESM3-6). Porphyroclastic group tend to have higher MgO contents with respect to Protogranular group. TiO_2 and Al_2O_3 positive correlation would depend upon melt extraction (Takazawa et al., 2000; Ionov, 2007). However, considering our data together with those of Vaselli et al. (1995) and with only few exceptions, these samples have less FeO with respect to the expected Al_2O_3 content, this latter being even higher with respect to the corresponding MgO predicted by models for any kind of melting evolution (ESM3-7), both at constant and decreasing P (Niu, 2004; Ishimaru et al., 2007). Thus, the extremely Al_2O_3-rich compositions of some PMVF mantle xenoliths cannot be explained by partial melting alone.

Similar information is given by mineral phase composition. Johnson et al. (1990) proposed the most used, mineral-focused model to predict the melting degree for batch and fractional melting, based on cpx REE patterns, while more recently Scott et al. (2016) proposed a similar approach for opx. Bonadiman and Coltorti (2018) attempted to infer the partial melting degree of a mantle lithotype based on major element composition of olivine, opx, cpx and spinel. As is well known, cpx is the most important incompatible trace element repository within an anhydrous peridotite, constraining the overall REE budget. Obviously this is not true when a volatile-bearing phase is present, taking into account that amphibole partitioning coefficients are higher than those of cpx for most incompatible elements (Ionov et al., 1997; Witt-Eickschen and Harte 1994). Disseminated amphibole is common within the PMVF xenoliths, with trace element patterns perfectly mimicking those of cpx apart from elements which are preferentially incorporated in the amphibole crystal lattice (Figs. 6, 7, 8). The ubiquitous similarity between the trace element patterns of the two minerals - regardless of textural positions or presence of an amphibole vein - is a strong indication

of disseminated amphibole genesis via cpx hydration, followed by subsolidus re-equilibration. Since amphibole grew over cpx, some differences should be expected between cpx patterns in anhydrous and hydrous parageneses. However, the patterns of cpx from anhydrous lherzolite BARQ4 are identical to those of cpx from lherzolites LAG21 and LAG24, having 0.7 and 1% of modal disseminated amphibole, respectively. For this reason, no re-distribution modeling backward from amphibole to cpx has been developed and we assumed that the trace element contents of cpx correspond to the original composition, i.e. should represent a suitable indicator of the partial melting degree (F%). Batch, fractional and incremental (with 1% increment for each step) melting modeling were thus developed following the Johnson et al. (1990) equations, using as starting composition the primordial, fertile cpx proposed by Bonadiman et al. (2005) for spinel peridotites. The best fit between model and real cpx was obtained for fractional melting (ESM3-8), although many of the samples (BARQ4, LAG21, LAG24, LAG51, TRE4) have HREE and MREE values higher than those of the primordial cpx, while LREE can be variably enriched or depleted. Cpx from lherzolite LAG52 perfectly overlaps the pattern of primordial cpx, while LAG1, TRE1 and TRE2 indicate very low degrees of partial melting, between 1 and 5 %. Thus, according to cpx REE composition, PMVF xenoliths represent a very fertile mantle that, however, cannot be explained just invoking low-degree melting processes. This conclusion is further supported by investigating the opx. According to the model of Scott et al., (2016), opx REE patterns indicate substantially higher degrees of melting (ESM3-9). The comparison has been developed based on HREE (since LREE are highly variable and more prone to be modified by post-melting processes) and taking into account that the model starts from the DMM source by Workman and Hart (2005), already slightly depleted by 2-4 % melt extraction. Protogranular group opx would have been affected by a melting event between 12 and 20%, whereas Porphyroclastic group opx would record 20 to 25% melting, with TRE1 being the most depleted. Using the approach developed by Bonadiman and Coltorti (2018) in the CMAS-Fe system for pressures varying between 1 to 3 GPa and temperatures between 900 and 1300 °C, (which also takes into account subsolidus re-equilibration), the opx major element

composition indicates rather low degrees of partial melting (mainly < 15%), although the fit with the theoretical curve is rather limited (Fig. 3A). The indication of low degree of melting comes from the high Al_2O_3 contents that in some samples (LAG24, LAG2 and TRE3) is higher than that of a primordial opx. As far as mg# is concerned, some samples shift toward higher values while others, including LAG52 (the only one with an amphibole vein) towards lower values with respect to the theoretical curve, at constant Al_2O_3 value. Taking into account the existing Fe and Mg equilibrium between opx and olivine, as well as the Fo and NiO content of the latter - unlikely for low degree of melting - it can be hypothesized that Al_2O_3 has been added to the system after partial melting. If this is the case and the opx composition is reported on the curve following the mg#, the obtained degrees of melting appear more similar to those estimated from the HREE in opx. Support for this comes from the composition of primary (and secondary) opx in xenoliths from mantle wedges from Kamchatka, Philippines and Cascade Range (Fig. 3A). These opx fall at the bottom of the theoretical line and have high mg# - similar to those of TRE1 – coupled with very low Al_2O_3 contents. It is then reasonable to suggest that PMVF xenoliths were residua of partial melting degrees comparable to those of typical sub-arc mantle that was later affected by Al_2O_3 enrichment. The event would have also increased the modal percentage of opx, which explains why some PMVF xenoliths have a paragenesis moving toward ol-websterites, with modal opx contents up to 36.2%, much higher than that of fertile mantle (25%, Johnson et al., 1990). A SiO_2-saturated, Al_2O_3-rich metasomatizing melt could increase the opx modal content with mg# buffered by the matrix, concomitantly with, or followed by, textural re-equilibration and re-crystallization. This reorganization could have occurred under the stress regime consequent to slab steepening/sinking and to asthenosphere uprise that pushed the overlying lithospheric mantle column upward (Falus et al., 2000, 2008, 2011). Enhanced recrystallization of newly formed ("secondary") opx in a mantle wedge can completely obliterate its initial replacement texture so that it looks like a primary phase (Arai and Ishimaru, 2008).

A similar interpretation can be put forward for cpx major elements, having mg# values compatible with melting degrees $\geq$ 20%, but showing Al_2O_3 contents higher than those expected by theoretical calculations. Thus their Mg and Fe contents, being buffered by the matrix, can be considered as good indicators of the partial melting degree, while Al_2O_3 and REE are probably related to the enrichment process. As for opx, in Fig. 2A the composition of cpx from various subarc settings is reported. In all cases, cpx with mg# equal or exceeding the degree of partial melting after which this phase is exhausted (F= 22-25%, Bernstein et al., 2007; Sobardere et al., 2018) are found, but PMVF cpx show significant Al_2O_3 enrichment with respect to the theoretical curve. It is likely that these cpx were newly formed, growing over strongly depleted cpx in an originally harzburgitic matrix (which buffered the mg#) from an Al_2O_3-rich melt. Alternatively, cpx could have been generated by exsolution from opx and successively texturally re-organized and enriched by an Al_2O_3-rich metasomatizing melt. In the Protogranular group it is evident that cpx are newly formed, with Al_2O_3 and modal content exceeding the PM values. A similar observation is valid for the Porphyroclastic group that, however, does not show an analogous level of enrichment. Cpx from anhydrous harzburgite TRE1 have the highest mg# and the lowest Al_2O_3 content, probably because this sample was less affected by the enrichment process and/or started from the most residual composition.

In this framework, the metasomatic process that affected the mantle beneath the Persani Mts. can be more properly considered as a refertilisation that not only modified the composition of the various phases, but also consistently increased the pyroxene modal abundance. Pyroxenes increased at expenses of olivine, as observed by Falus et al. (2008). Spinel was also most probably enriched and/or added to the peridotitic matrix during the refertilisation, as testified by its modal abundance, up to 5.3 % in some samples (Table 1 ESM), and very high Al_2O_3 content (ESM3-2).

In order to further decipher this history, we compared ^4He and $^{40}Ar^*$ concentrations and $^4He/^{40}Ar^*$ in FI with the mg# (Fig. 12). In a recent study from Lower Silesia mantle xenoliths, Rizzo et al. (2018) showed that the chemistry of FI and minerals coupled to $^4He/^{40}Ar^*$ ratio may provide insights into the extent of partial melting, as well as the occurrence of metasomatic processes that

masked the pristine SCLM characteristics. This is related to the different crystal–melt partitioning of ^{4}He and $^{40}Ar^{*}$ for olivine and cpx (Heber et al., 2007).

Olivine in the PMVF xenoliths are the most useful phase for identifying the residual mantle through $^{4}He/^{40}Ar^{*}$, bearing in mind that increasing mg# should indicate higher extent of partial melting, leading to a depleted lithology (Herzberg et al., 2016; Rizzo et al., 2018). In the few samples not affected by diffusive fractionation (LAG52, BARQ4, TRE2), a progressive decrease of ^{4}He and $^{40}Ar^{*}$ concentrations at increasing mg# (from 89.2 to 90.7) can be noticed (Fig. 15), which is compatible with partial melting. This is supported by the $^{4}He/^{40}Ar^{*}$ ratio that decreases from 2.2 to 1.4 at increasing mg#, being $^{4}He/^{40}Ar^{*}$ within the reported range for mantle production, indicating a rather low partial melting degree. For comparison, olivine from the Lower Silesia mantle with a $^{4}He/^{40}Ar^{*}$ ~0.3, record a residual mantle that was strongly depleted (25–30% of partial melting, Rizzo et al., 2018). Alternatively, we may suppose that olivine recrystallized during or after a metasomatic/refertilisation process by trapping FI with $^{4}He/^{40}Ar^{*}$ typical of mantle production. If so, we would not have any trace of primary FI resembling the residual mantle features.

Looking at opx and cpx, most of the samples do not show any relation between ^{4}He, $^{40}Ar^{*}$ concentrations, $^{4}He/^{40}Ar^{*}$ ratios and mg# (Fig. 12). The only exception is LAG52 that has the highest ^{4}He and $^{40}Ar^{*}$ concentrations at the lowest mg#, compatible with low extent of partial melting relative to the other samples; however, in terms of $^{4}He/^{40}Ar^{*}$ this sample has not the highest values (Fig. 12), as would be expected if partial melting was the main process. This means that LAG52 did not maintain memory of the melting history. In terms of $^{4}He/^{40}Ar^{*}$, opx and cpx show $^{4}He/^{40}Ar^{*}$ values in the range 0.2-1.2, without any significant trend. Apart from sample TRE3, opx and cpx have $^{4}He/^{40}Ar^{*}>0.6$. These values are not compatible with the degrees of melting estimated by using mineral chemistry. This behaviour suggests that most of the opx and cpx recrystallized, as consequence of refertilisation, by trapping a new population of FI with a distinct composition that masked the previous partial melting history.

6.5 Refertilisation geodynamic context and subsequent alkaline metasomatism

The geochemical affinity of the refertilizing melt can be evaluated thanks to the presence of disseminated amphibole. According to Coltorti et al. (2007b), the geochemical imprint of a metasomatizing agent can be traced back by using key elements (particularly Nb and in general the HFSE, which are highly immobile during chromatographic fractionation, Ionov et al., 2002) and their ratios. In Zr/Nb vs Ti/Nb (Fig. 13A) and Zr/Nb vs Ti/Zr (Fig. 13B) diagrams, disseminated amphiboles fall entirely within the "subduction-related" field, indicating that they were generated by a subduction-related melt. The sinking oceanic slab is still visible today as evidenced by geophysical surveys under the seismically active Vrancea Zone in the southeastern edge of the Carpathian arc (Ismail-Zadeh et al., 2012). Post-collisional magmatism along the East Carpathian range migrated and rejuvenated from the NW, where the oldest occurrences are found (10.2 Ma), to SE in the South Harghita volcanic field, where the activity is younger than 1 Ma (Seghedi et al., 2016, 2019). The South Harghita calc-alkaline volcanic activity was the last expression of a post-collisional, convergent margin dynamic. Asthenospheric upwelling, linked to slab roll-back, was associated with extensional Na and K-alkaline volcanism (Seghedi et al., 2011). The last eruptive phase of Perşani Mts. occurred contemporaneously with the final stages of South Harghita volcanic activity around 0.6 Ma (Pécskay et al., 1995b; Molnar et al., 2018). Although calc-alkaline products do not outcrop in the Perşani Mts, a cognate basaltic block found within the pyroclastic deposits shows a clear subduction-related signature (sample Lgf in Downes et al., 1995) and is identical to some Călimani-Ghurghiu-Harghita (CGH) basaltic andesites (ESM3-10), supporting the idea that, also in this area, a calc-alkaline magmatic phase (now buried) preceded the alkaline stage.

It is thus likely that the mantle beneath Perşani Mts. interacted with calc-alkaline magmas and maybe the majority of melt volumes were trapped and consumed at depth during the refertilisation process. The most primitive magmas in the Călimani-Gurghiu-Harghita volcanic chain have Al_2O_3 contents ranging between 16 and 21 wt%, MgO around 5 wt%, and Y as high as 28 ppm (Mason et al., 1996). One of these magmas is considered as the parental melt of the Călimani series, with

$^{87}Sr/^{86}Sr$ and $^{143}Nd/^{144}Nd$ ratios of 0.70525 and 0.51275, respectively, explained by the authors as the result of slight AFC processes that occurred within the crust or, alternatively, of sediment subduction and consequent source contamination. Such a composition fits reasonably well the requirements of the melt responsible for the mantle refertilisation recorded in PMVF mantle xenoliths.

Disseminated amphiboles clearly have a subduction-related origin while the amphibole vein of lherzolite LAG52 falls in the intraplate field (Fig. 13A, B), showing a striking resemblance with amphibole megacrysts collected in the pyroclastic deposits of the Perşani Mts (Fig. 14). Continuous variation trends from vein amphiboles to megacrysts can be observed, with a constant decrease in mg#, Al_2O_3, Na_2O and Cr_2O_3 and an increase in TiO_2 (Fig. 4B) and K_2O. Oxygen and δD isotopic composition of megacrysts from Perşani and from the Carpathian-Pannonian region support their mantle origin. They are interpreted as fractionation product of basaltic melts (similar to the host alkali basalts, Zanetti et al., 1995) derived by various degrees of partial melting of an asthenospheric source contaminated by fluids released from subducted serpentinites or blueschist like those occurring in the Meliata-Vardar series (Demény et al., 2012).

Interaction of PMVF mantle with alkaline melts has been already documented and there is good agreement that amphibole vein generation is the main result of this process. Olivine-clinopyroxenites also found as xenoliths in the Perşani Mts volcanics probably represent fractionation products of these alkaline melts formed at depth, within the mantle (Zanetti et al., 1995; Vaselli et al., 1995; Chalot-Prat & Boullier 1997; Downes, 2001). Since the disseminated amphiboles are the result of reaction/hydration of cpx, it has to be concluded that the two kinds of amphibole represent different metasomatic episodes that occurred at different times. Since the interaction with calc-alkaline magmas occurred first, we argue that vein amphibole generation was subsequent to the formation of disseminated amphiboles and may represent the last metasomatic event recorded by PMVF mantle xenoliths. According to Zanetti et al. (1995), some vein amphiboles may represent the "frozen" composition of the alkaline magma travelling through the

mantle (Fig. 14). Beside the variable enrichments in LREE, chondrite-normalized REE patterns of LAG52 vein amphiboles are very similar to those found in the literature, including amphiboles of clinopyroxenites and megacrysts. Although the explanation by Zanetti et al. (1995) may be realistic, adcumulates are unlikely to perfectly match a liquid composition (Holness et al., 2017) and vein amphibole are indeed lower in L- and MREE with respect to Perşani Mts lavas. We have thus calculated the melt in equilibrium with LAG52 vein amphibole using $Kd^{amph/alkaline\ melt}$ from the GERM database and the result was almost indistinguishable from the real Perşani Mts. alkaline magmas. Calculated cpx in equilibrium with the obtained melt (Fig. 15) is identical to the real cpx from PMVF clinopyroxenites (Vaselli et al., 1995; Chalot-Prat & Boullier, 1997). It has to be underlined that both natural and calculated cpx have completely different compositions, in term of major and trace elements, with respect to those occurring in the refertilized mantle xenoliths. The "magmatic" cpx derived from the alkaline melt/s have different REE patterns (in particular higher LREE and lower HREE, Fig. 15) with respect to the peridotitic ones and could have never been generated by the same liquid. Even using a chromatographic model (Ionov et al., 2002), we could not obtain such HREE-enriched diopsides (Yb up to 18.7 x Chondrite) starting from the alkaline cpx (Yb, 7.4 x Chondrite) supposing that the alkaline melt was the sole metasomatic agent that acted within the PMVF mantle. This further supports the hypothesis that cpx and disseminated amphiboles are closely related and are the result of a previous, calc-alkaline, extremely pervasive refertilisation event, distinct from the subsequent alkaline metasomatic episode. The latter, on the other hand, resulted in the generation of amphibole veins within the peridotite and in the crystallization of amphibole-bearing clinopyroxenites and megacrysts. These magmas, very similar to those erupted by the Persani Mts. volcanoes and generated by a new source, crossed the lithospheric mantle section in more recent times (most probably after the onset of post-collisional tectonics) at relatively shallow depth, reached as a consequence of asthenosphere doming. This allowed vein formation with very limited diffusive effects, only detectable as slight LREE and Nb enrichments in some of the pre-existing pyroxenes and their associated amphiboles (Group 2 and 3,

Figs. 6 and 8), especially in close proximity to the amphibole vein. The influence of this last alkaline metasomatic event also left trace in the FI noble gases composition of some samples. TRE1, TRE2 and TRE4 have mg# > 90.9 and $^{4}He/^{40}Ar^{*}$ between 1.3 and 2.5 (Fig 12), showing a gradual increase of mg# and $^{4}He/^{40}Ar^{*}$ that cannot be explained by either partial melting or refertilisation, due to their strong depletion. The most reasonable explanation for the FI chemistry of these samples involves the entrapment of secondary FI from the latest alkaline metasomatism or from the host magma that resemble more "magmatic-like" $^{4}He/^{40}Ar^{*}$ values. This interpretation is further supported by the $^{3}He/^{4}He$ values (6.5-6.8 Ra), which are clearly higher than the other opx (5.4-6.4 Ra) and cpx (5.3-6.1) as well as of olivine (5.2-5.9 Ra) (Fig. 12). Two of these samples belong to the low-temperature, high-stress *Po. s.s.* textural sub-group (Table 1), probably more prone to fluid percolation. We argue that the $^{3}He/^{4}He$ signature of fluids trapped in opx and cpx of samples TRE1, TRE2 and TRE4 can be related to MORB-like asthenospheric fluids that penetrated the local mantle and partially mixed with residual fluids contaminated by the recycling of crustal (subduction-related) material.

In summary, the comparison of FI and mineral chemistry mostly points toward a mantle originally depleted by rather high extents of partial melting and then re-fertilized by subduction-related fluids. A small portion of the mantle also bears a memory of the latest alkaline metasomatism or the infiltrated host magma.

6.6 Subduction of crustal material and the origin of alkaline magmatism

In order to make inferences on the noble gas signature of SCLM beneath PMVF, we now focus on the He and Ne isotope compositions and compare them with other European localities.

The range of $^{3}He/^{4}He$ measured in olivine (only three reliable measures from LAG52, BARQ4 and TRE2), opx and cpx (excluding samples TRE1, TRE2, and TRE4) is 5.8±0.2 Ra (Figs. 10, 12 and ESM3-11). This range is comparable to the few $^{3}He/^{4}He$ measurements for xenoliths from PMVF analysed with a crushing technique, which yielded 5.6 and 6.0 Ra (Althaus et al., 1998; Kis et al.,

2019). This suggests that the mantle beneath PMVF has $^{3}He/^{4}He$ values more radiogenic than the typical MORB source (8±1 Ra; Graham, 2002), and among the most radiogenic within the European SCLM range (6.3±0.4 Ra; Gautheron et al., 2005; Martelli et al., 2011; Rizzo et al., 2018) together with xenoliths from Tallante (Spain) that give 5.6±0.1 Ra (Figs. 10 and 12).

Gautheron et al. (2005) justified the average $^{3}He/^{4}He$ signature of the European SCLM, proposing two interpretations: i) a recent and local metasomatism by a MORB-like He composition rising from the asthenosphere and mixing with a more-radiogenic isotope signature produced in the lithosphere or ii) a global SCLM steady state in which a flux of ^{3}He-rich fluids originated from the asthenosphere mixed with ^{4}He-rich fluids/melts recycled in the lithosphere from U-Th decay of crustal material. This material could be derived from dehydration of active or fossil subducting slabs (e.g., Yamamoto et al., 2004; Faccenna et al., 2010).

Therefore, the $^{3}He/^{4}He$ signature of mantle beneath the PMVF can be interpreted with the models proposed by Gautheron et al. (2005), assuming an enhanced recycling of crustal material in the local lithosphere with respect to other European areas.

The low noble gases (and CO_2) concentrations, as well as the lower $^{3}He/^{4}He$ in PMVF mantle xenoliths compared to other parts of the European SCLM (Gautheron et al., 2005; Rizzo et al., 2018), support a subduction-related imprint of fluids recycled in the local mantle at the time of re-fertilization.

The apparent paradox between a fluid/sediments-rich environment, and the low concentration of noble gases, could be reconciled by inferring that these fluids were richer in H_2O than in CO_2. Because CO_2 is the main carrier of noble gases at whatever depth of circulation (i.e., mantle or crust; Anderson, 1998), this could explain the low ^{4}He and $^{40}Ar^{*}$ concentrations in FI from PMVF. The diffusive fractionation of noble gas observed in these mantle portions could also suggest a continue mantle recrystallization due to the stresses related to asthenospheric upwelling.

Neon isotope ratios give similar indications to the $^{3}He/^{4}He$ ratios. Fig. 9 shows that PMVF $^{21}Ne/^{22}Ne$ and $^{20}Ne/^{22}Ne$ plot along or slightly below the theoretical mixing line between air and a

MORB-like mantle. Data slightly below this mixing line can be interpreted as indicating a three component mixing that includes crustal material (Kennedy et al., 1990; Ballentine, 1997; Ballentine et al., 2005). This supports the idea based on $^{3}He/^{4}He$ ratios that the mantle beneath the PMVF was metasomatized/refertilized by subduction-related fluids that were responsible for recycling of crustal material in the local SCLM, but the time of this event is not yet known.

Finally, the evidence from He and Ne isotope compositions precludes the presence of a plume below the PMVF. A plume-related signature should have $^{3}He/^{4}He$ values above the MORB range (>9 Ra) and a lower $^{21}Ne/^{22}Ne$ ratio for a given $^{20}Ne/^{22}Ne$ than MORB melts (Kurz et al., 2009; Moreira, 2013) (Figs. 10 and 9). However, the ranges of He and Ne isotope ratios are similar to those for other European regions where no plume is present (Gautheron et al., 2005; Moreira et al., 2018).

6.7 Comparison with gases emitted in the Eastern Carpathians

In the south-eastern Carpathian-Pannonian Region, anorogenic or orogenic magmas have been erupted since 11 Ma (Szakács et al., 1993; Seghedi et al., 2004, 2011). Although volcanic activity in the PMVF may now be extinct strong CO_2 degassing in the neighbouring Ciomadul volcanic area (about 40 km to the east) may indicate that magma is still present (Oncescu et al., 1984; Althaus et al., 2000; Vaselli et al., 2002; Popa et al., 2012; Kis et al., 2017, 2019; Laumonier et al., 2019). Many gas emissions are present, emitting a huge amount of CO_2 (8.7×10^{3} t/y) similar to other >10 kyr dormant volcanoes worldwide (Kis et al., 2017). These gas manifestations are the closest to the outcrops containing mantle xenoliths for comparison of the noble gas composition. $^{3}He/^{4}He$ values from Stinky Cave (Puturosul), Doboşeni and Balvanyos are up to 3.2, 4.4 and 4.5 Ra, respectively, indicating the presence of cooling magma (Althaus et al., 2000; Vaselli et al., 2002).

In the Ciomadul area, Kis et al. (2019) measured $^{3}He/^{4}He$ ratios up to 3.1 Ra, arguing that these values indicate a mantle lithosphere strongly contaminated by subduction-related fluids and post-metasomatic ingrowth of radiogenic ^{4}He. In contrast with Kis et al. (2019) we consider it more

likely that magmatic gases from Ciomadul volcano are not representative of the local mantle but are being released from a cooling and aging magma that resides within the crust (see also Laumonier et al, 2019). Alternatively, magmatic gases are contaminated by crustal fluids while they are rising to the surface, as proposed by Althaus et al. (2000) and Vaselli et al. (2002).

7. CONCLUSIONS

The lithospheric mantle beneath the Eastern Transylvanian Basin was investigated through a suite of ultramafic xenoliths mainly composed of lherzolites, extremely fertile (cpx modal content up to 22%) and characterized by the almost ubiquitous presence of disseminated amphibole and a continuous textural variation from recrystallized protogranular to porphyroclastic types.

Petrographic features, whole rock and mineral chemistry and noble gases (He, Ne, Ar) in FI reveal a complex evolution of this mantle section. Porphyroclastic samples still bear clues of variable degrees of partial melting, as testified by high mineral mg# and depleted opx M-HREE patterns. On the other hand, the high cpx modal contents and the Al_2O_3 contents and REE patterns of the pyroxenes in the protogranular samples are not compatible with simple melting processes, but can be explained by a pervasive refertilisation event that erased, in most cases, the evidence of the pristine depleted parageneses. The high Al_2O_3 contents of pyroxenes and spinel and the HFSE ratios of disseminated amphiboles point toward a calc-alkaline nature for the refertilizing magma that was similar to the most primitive basalts of the Călimani series. Further support to this hypothesis derives from the finding, within PMVF pyroclastic sequences, of a lithic cognate of calc-alkaline affinity 1Ma older than the alkali basalts and similar to some basaltic andesites of the CGH chain. The studied mantle section also shows evidence of interaction with melts of different kind, visible from slight LREE enrichment in pyroxenes and amphibole vein formation. This metasomatic event is linked to the passage of alkaline melts similar to the host lavas, as testified by the close resemblance between the amphibole vein and the megacrysts also found in the Perşani Mts pyroclastic deposits.

In the PMVF xenoliths, FI are mostly secondary. The isotope compositions of Ne and Ar and, complementarily, the $^{4}He/^{20}Ne$ ratio highlights a variable air contamination, progressively decreasing from olivine to cpx. This contamination seems to be a local mantle feature inherited from the recycling of subduction-related fluids, during the last orogenic event in Eastern Carpathians. Excluding data modified by diffusive fractionation, the comparison of ^{4}He and $^{40}Ar^{*}$ concentrations as well as $^{4}He/^{40}Ar^{*}$ with the mg# of olivine, opx and cpx does not show clear variations due to partial melting. Most of the pyroxenes recrystallized, because of refertilisation by subduction-related melts. A small portion of the mantle also carries a memory of the latest alkaline metasomatism or the host magma, as testified by $^{4}He/^{40}Ar^{*}$ and $^{3}He/^{4}He$ values in those samples more texturally prone to fluid infiltration. Excluding these latter, the range of $^{3}He/^{4}He$ measured in olivine, opx and cpx is 5.8±0.2 Ra, which is more radiogenic than the typical MORB mantle (8±1 Ra) and among the lowest values found in western and central European volcanic provinces (6.3±0.4 Ra). We argue that the $^{3}He/^{4}He$ signature of mantle beneath the PMVF reflects a greater amount of recycling of crustal material in the local lithosphere compared to other European portions. Ne isotope ratios give indications similar to the $^{3}He/^{4}He$ ratio, with $^{21}Ne/^{22}Ne$ and $^{20}Ne/^{22}Ne$ data plotting along, or slightly below, the theoretical mixing line between air and a MORB-like mantle. The evidence from He and Ne isotope compositions exclude the presence of a plume below the PMVF.

Comparing the xenolith $^{3}He/^{4}He$ signature with that of CO_2-dominated gas emissions around Ciomadul subduction-related volcanic complex (up to 4.5 Ra), located only about 40 km to the east of our study area, we conclude that surface gases are not representative of the local mantle. Rather, they are released from a cooling and aging magma residing within the crust or, alternatively, they are contaminated by crustal fluids during their rise toward the surface.

ACKNOWLEDGMENTS

The project was funded by the Italian National Research Program [PRIN_2017 Project 20178LPCPW] to M.C. The noble gas contribution in this work is part of the PhD (XXXII cycle) of A. L. R. at the University of Ferrara. We thank Mariagrazia Misseri and Mariano Tantillo for helping in samples preparation, isotope analysis of noble gases and laboratory activities. I.S. was supported by grant of Ministry of Research and Innovation, CNCS – UEFISCDI, project number PN-III-P4-ID-PCCF-2016-4-0014, within PNCDI III. Helpful suggestions by Hilary Downes and an anonymous reviewer greatly improved the manuscript.

8. REFERENCES

Abe, N., Arai, S., Yurimoto, H., 1998. Geochemical characteristics of the uppermost mantle beneath the Japan island arcs; implications for upper mantle evolution. Physics of the Earth and Planetary Interiors 107, 233-46.

Althaus, T., Niedermann, S., Erzinger, J., 1998. Noble gases in ultramafic mantle xenoliths of the Persani Mountains, Transylvanian Basin, Romania. Goldschmidt Conference Toulouse 1998 Abstract book, Mineralogical Magazine 62A.

Althaus, T., Niedermann, S., Erzinger, J., 2000. Noble gas studies of fluids and gas exhalations in the East Carpathians, Romania. Chemie der Erde 60, 189–207.

Anderson, D.L., 1998. A model to explain the various paradoxes associated with mantle noble gas geochemistry. Proceedings of the National Academy of Sciences USA 95, 9087-9092.

Arai, S., Ishimaru, S., Okrugin, V.M., 2003. Metasomatized harzburgite xenoliths from Avacha volcano as fragments of mantle wedge of the Kamchatka arc: Implication for the metasomatic agent. The Island Arc 12, 233-246.

Arai, S., Takada, S., Michibayashi, K., Kida, M., 2004. Petrology of peridotite xenoliths from Iraya Volcano, Philippines, and its implication for dynamic mantle-wedge processes. Journal of Petrology 45, 369-389.

Arai, S., Ishimaru, S., 2008. Insights into petrological characteristics of the lithosphere of mantle wedge beneath arcs through peridotite xenoliths: a review. Journal of Petrology 49, 665–695.

Ballentine, C.J., 1997. Resolving the mantle He/Ne and crustal $^{21}Ne/^{22}Ne$ in well gases. Earth and Planetary Science Letters 152, 233–249.

Ballentine, C.J., Marty, B., Sherwood Lollar, B., Cassidy, M., 2005. Neon isotopes constrain convection and volatile origin in the Earth's mantle. Nature 433, 33–38.

Ballhaus, C., Berry, R.F., Green, D.H., 1991. High pressure experimental calibration of the olivine-orthopyroxene-spinel oxygen barometer: implications for the oxidation state of the mantle. Contribution to Mineralogy and Petrology 107, 27-40.

Bénard, A., Woodland, A.B., Arculus, R.J., Nebel, O., McAlpine, S.R.B., 2018. Variation in sub-arc mantle oxygen fugacity during partial melting recorded in refractory peridotite xenoliths from the West Bismarck Arc. Chemical Geology 486, 16-30.

Bernstein, S., Kelemen, P.B., Hanghoj, K., 2007. Consistent olivine Mg# in cratonic mantle reflects Archean mantle melting to the exhaustion of orthopyroxene. Geology 35, 459-462.

Bianchini, G., Beccaluva, L., Nowell, G.M., Pearson, D.G., Siena, F., 2011. Mantle xenoliths from Tallante (Betic Cordillera): Insights into the multi-stage evolution of the south Iberian lithosphere. Lithos 124, 308-318.

Bonadiman, C., Beccaluva, L., Coltorti, M., Siena, F., 2005. Kimberlite-like metasomatism and 'garnet signature' in spinelperidotite xenoliths from Sal, Cape Verde Archipelago: relics of a subcontinental mantle domain within the Atlantic Oceanic lithosphere? Journal of Petrology 46, 2465-2493.

Bonadiman, C., Coltorti, M., 2018. Mantle subsolidus and melting behavior as modelled in the system CMASFe. 3rd European Mantle Workshop, Pavia, June 26-28, 2018, Abstract Book.

Brandon, A.D., Draper, D.S., 1996. Constraints on the origin of the oxidation state of mantle overlying subduction zones: an example from Simcoe, Washington, USA. Geochimica et Cosmochimica Acta 60, 1739–1749.

Brey, G.P., Köhler, T., 1990. Geothermobarometry in the four-phase lherzolites II. New Thermobarometers and practical assessment of existing thermobarometers. Journal of Petrology 31, 1353-1378.

Bryant, J.A., Yogodzinsky, G.M., Churikova, T.G., 2007. Melt-mantle interactions beneath the Kamchatka arc: evidence from ultramafic xenoliths from Shiveluch volcano. Geochemistry Geophysics Geosystems 8, Q04007, doi:10.1029/2006GC001443, ISSN: 1525-2027.

Burnard, P.G., Farley, K., Turner, G., 1998. Multiple fluid pulses in a Samoan harzburgite. Chemical Geology 147, 99–114.

Burnard, P., 2004. Diffusive fractionation of noble gases and helium isotopes during mantle melting. Earth and Planetary Science Letters 220, 287–295.

Chalot-Prat, F., Bouillier, A-M., 1997. Metasomatism in the subcontinental mantle beneath the Eastern Carpathians (Romania): new evidence from trace element geochemistry. Contribution to Mineralogy and Petrology 129, 284-307.

Coltorti, M., Bonadiman, C., Faccini, B., Ntaflos, T., Siena, F., 2007a. Slab melt and intraplate metasomatism in Kapfenstein mantle xenoliths (Styrian Basin, Austria). Lithos 94, 66-89.

Coltorti, M., Bonadiman, C., Faccini, B., Grégoire, M., O'Reilly, S.Y., Powell, W., 2007b. Amphiboles from suprasubduction and intraplate lithospheric mantle. Lithos 99, 68-84.

Créon, L., Rouchon, V., Youssef, S., Rosenberg, E., Delpech, G., Szabó, C., Remusat, L., Mostefaoui, S., Asimow, P. D., Antoshechkina, P. M., et al., 2017. Highly CO_2-supersaturated melts in the Pannonian lithospheric mantle – A transient carbon reservoir? Lithos 286–287, 519–533.

Demény, A., Vennemann, T.W., Homonnay, Z., Milton, A., Embey-Isztin, A., Nagy, G., 2005. Origin of amphibole megacrysts in the Pliocene-Pleistocene basalts of the Carpathian-Pannonian region. Geologica Carpathica 56, 179-189.

Demény, A., Harangi, S., Vennemann, T.W., Casillas, R., Horvát, P., Milton, A.J., Mason, P.R.D., Ulianov, A., 2012. Amphiboles as indicators of mantle source contamination:

Combined evaluation of stable H and O isotope compositions and trace element ratios. Lithos 152, 141-156.

Downes, H., Seghedi, I., Szakács, A., Dobosi, G., James, D.E., Vaselli, O., Rigby, I.J., Ingram, G.A., Rex, D., Pécskay, Z., 1995. Petrology and geochemistry of the late Tertiary/Quaternary mafic alkaline volcanism in Romania. Lithos 35, 65–81.

Downes, H., 2001. Formation and modification of the shallow sub-continental lithospheric mantle: a review of geochemical evidence from ultramafic xenolith suites and tectonically emplaced ultramafic massifs of Western and Central Europe. Journal of Petrology 42, 233-250.

Edwards, M.A., Grasemann, B., 2009. Mediterranean snapshots of accelerated slab retreat: subduction instability in stalled continental collision. Geological Society, London, Special Publication 311, 155-192.

Embey-Isztin, A., Dobosi, G., Altherr, R., Meyer, H.-P., 2001. Thermal evolution of the lithosphere beneath the western Pannonian Basin: evidence from deep seated xenoliths. Tectonophysics 331, 285-306.

Faccenna, C., Becker, T.W., Lallemand, S., Lagabrielle, Y., Funiciello, F., Piromallo, C., 2010. Subduction-triggered magmatic pulses: a new class of plumes? Earth and Planetary Science Letters 299, 54–68.

Faccini, B., Bonadiman, C., Coltorti, M., Grégoire, M., Siena, F., 2013. Oceanic material recycled within the sub-Patagonian lithospheric mantle (Cerro del Fraile, Argentina). Journal of Petrology 54, 1211-1258.

Falus, G., Szabó, C., Vaselli, O., 2000. Mantle upwelling within the Pannonian Basin: evidence from xenolith lithology and mineral chemistry. Terra Nova 12, 295-302.

Falus, G., Tommasi, A., Ingrin, J., Szabó, C., 2008. Deformation and seismic anisotropy of the lithospheric mantle in the southeastern Carpathians inferred from the study of mantle xenoliths. Earth and Planetary Science Letters 272, 50–64.

Falus, G., Tommasi, A., Soustelle, V., 2011. The effect of dynamic recrystallization on olivine crystal preferred orientations in mantle xenoliths deformed under varied stress conditions. Journal of Structural Geology 33, 1528-1540.

Foley, S.F., 2011. A reappraisal of redox melting in the Earth's Mantle as a function of tectonic setting and time. Journal of Petrology 52, 1363-1391.

Forshaw, J.B., Waters, D.J., Pattison, D.R.M., Palin, R.M., Gopon, P., 2019. A comparison of observed and thermodynamically predicted phase equilibria and mineral compositions in mafic granulites. Journal of Metamorphic Geology 37, 153-179.

Gautheron, C., Moreira, M., Allègre, C., 2005. He, Ne and Ar composition of the European lithospheric mantle. Chemical Geology 217, 97–112.

Graham, 2002. Noble gas isotope geochemistry of Mid-Ocean Ridge and Ocean Island Basalts: characterization of mantle source reservoirs. Review of Mineralogy and Geochemistry 47, 247–317.

Harangi, S., Sági, T., Seghedi, I., Ntaflos, T., 2015. A combined whole-rock and mineral-scale investigation to reveal the origin of the basaltic magmas of the Perşani monogenetic volcanic field, Romania, eastern-central Europe. Lithos 180–181, 43-57.

Harangi, S., Jankovics, M. É., Sági T., Kiss B., Lukács R., Soós I., 2014. Origin and geodynamic relationships of the Late Miocene to Quaternary alkaline basalt volcanism in the Pannonian Basin, eastern–central Europe. International Journal of Earth Sciences (Geol Rundsch) 104, 2007-2032.

Heber, V.S., Brooker, R.A., Kelley, S.P., Wood, B.J., 2007. Crystal-melt partitioning of noble gases (helium, neon, argon, krypton, and xenon) for olivine and clinopyroxene. Geochimica et Cosmochimica Acta 71, 1041–1061.

Heber, V.S., Wieler, R., Baur, H., Olinger, C., Friedmann, A., Burnett, D.S., 2009. Noble gas composition of the solar wind as collected by the Genesis mission. Geochimica et Cosmochimica Acta 73, 7414–7432.

Herzberg, C., Vidito, C., Starkey, N.A., 2016. Nickel–cobalt contents of olivine record origins of mantle peridotite and related rocks. American Mineralogist 101,1952–1966.

Holness, M.B., Vukmanovic, Z., Mariani, E., 2017. Assessing the role of compaction in the formation of adcumulates: a microstructural perspective. Journal of Petrology 58, 643-674.

Jamieson, H.E., Roeder, P.L., 1984. The distribution of Mg and Fe^{2+} between olivine and spinel at 1300°C. American Mineralogist 69, 283-291.

Johnson, K.T.M., Dick, H.J.B., Shimizu, N., 1990. Melting in the oceanic upper mantle: an Ion Microprobe study of diopsides in abyssal peridotites. Journal of Geophysical Research 95, 2661-2678.

Kennedy, B.M., Hiyagon, H., and Reynolds, J.H., 1990. Crustal neon: a striking uniformity. Earth and Planetary Science Letters 98, 277-286.

Kepezhinskas, P., Defant, M.J., Drummond, M.S., 1996. Progressive enrichment of island arc mantle by metl-peridotite interaction inferred from Kamchatka xenoliths. Geochimica et Cosmochimica Acta, 60, 1217-1229.

Kis, B.M., Ionescu, A., Cardellini, A., Harangi, S., Baciu, C., Caracausi, A., Viveiros, F. 2017. Quantification of carbon dioxide emissions of Ciomadul, the youngest volcano of the Carpathian-Pannonian Region (Eastern-Central Europe, Romania). Journal of Volcanology and Geothermal Research 341, 119–130.

Kis, B.M., Caracausi, Palcsu, L., Baciu, C., A., Ionescu, A., Futó, I., Sciarra, A., Harangi, S. 2019. Noble gas and carbon isotope systematics at the seemingly inactive Ciomadul volcano (Eastern-Central Europe, Romania): evidence for volcanic degassing. Geochemistry, Geophysics, Geosystems, https://doi.org/10.1029/2018GC008153.

Koněcný, V., Kováč, M., Lexa, J., Šefara, J., 2002. Neogene evolution of the Carpatho-Pannonian region: an interplay of subduction and back-arc diapiric uprise in the mantle. EGU Stephan Mueller Special Publication Series 1, 105-123.

Kovács, I., Patkó, L., Falus, G., Aradi, L.E., Szanyi, G., Gráczer, Z., Szabó, C., 2018. Upper mantle xenoliths as sources of geophysical information: the Perşani Mts. area as a case study. Acta Geodaetica et Geophysica, https://doi.org/10.1007/s40328-018-0231-2.

Kurz, M.D., Curtice, J., Fornari, D., Geist, D., Moreira, M., 2009. Primitive neon from the center of the Galápagos hotspot. Earth and Planetary Science Letters 286, 23–34.

Ionov, D.A., Griffin, W.L., O'Reilly, S.Y., 1997. Volatile-bearing minerals and lithophile trace elements in the upper mantle. Chemical Geology 141, 153-184.

Ionov, D.A., Bodinier, J-L., Mukasa, S. B., Zanetti, A., 2002. Mechanism and sources of mantle metasomatism: major and trace element compositions of peridotite xenoliths from Spitsbergen in the context of numerical modelling. Journal of Petrology 43, 2219-2259.

Ionov, D.A., 2007. Compositional variations and heterogeneity in fertile lithospheric mantle: peridotite xenoliths in basalts from Tariat, Mongolia. Contribution to Mineralogy and Petrology 154, 455-477.

Ionov, D.A., 2010. Petrology of mantle wedge lithosphere: new data on supra-subduction zone peridotite xenoliths from the andesitic Avacha volcano, Kamchatka. Journal of Petrology 51, 327-361.

Ionov, D.A., Bénard, A., Plechov, P.Yu., Shcherbakov, V.D., 2013. Along-arc variations in lithospheric mantle compositions in Kamchatka, Russia: First trace element data on mantle xenoliths from the Klyuchevskoy Group volcanoes. Journal of Volcanology and Geothermal Research 263, 122–131.

Ishimaru, S., Arai, S., Ishida, Y., Shirasaka, M., Okrugin, V.M., 2007. Melting and Multi-stage Metasomatism in the Mantle Wedge beneath a Frontal Arc Inferred from Highly Depleted Peridotite Xenoliths from the AvachaVolcano, Southern Kamchatka. Journal of Petrology 48, 395-423.

Ismail-Zadeh, A., Matenco, L., Radulian, M., Cloetingh, S., Panza, G., 2012. Geodynamics and intermediate-depth seismicity in Vrancea (the south-eastern Carpathians): current state-of-the-art. Tectonophysics 530–531, 50–79.

Laumonier, M., Karakas, O., Bachmann, O., Gaillard, F., Lukács, R., Seghedi I., Menand, T., Harangi, S., 2019. Evidence for a persistent magma reservoir with large melt content beneath an apparently extinct volcano. Earth and Planetary Science Letters 521, 79-90.

Lehmann, J., 1983. Diffusion between olivine and spinel: Application to geothermometry Earth and Planetary Science Letters, 64,123-138.

Lustrino, M., Wilson, M., 2007. The circum-Mediterranean anorogenic Cenozoic igneous province. Earth-Science Reviews 81, 1–65.

Mandler, B.E., Grove, T.L., 2016. Controls on the stability and composition of amphibole in the Earth's mantle. Contribution to Mineralogy and Petrology 171:68.

Martelli, M., Bianchini, G., Beccaluva, L., Rizzo, A., 2011. Helium and argon isotopic compositions of mantle xenoliths from Tallante and Calatrava, Spain. Journal of Volcanology and Geothermal Research 200, 18–26.

Martin, M., Wenzel, F., CALIXTO Working Group, 2006. High-resolution teleseismic body wave tomography beneath SE Romania: II. Imaging of a slab detachment scenario. Geophysical Journal International 164, 579–595.

Mason, P.R.D., Downes, H., Thirlwall, M. F., Seghedi, I., Szakács, A., Lowry, D., Mattey, D., 1996. Crustal assimilation as a major petrogenetic process in the East Carpathian Neogene and Quaternary continental margin arc, Romania. Journal of Petrology 37, 927-959.

Matenco, L., Bertotti, G., Leever, K., Cloetingh, S., Schmid, S.M., Tărăpoancă, M., Dinu, C., 2007. Large-scale deformation in a locked collisional boundary: Interplay between subsidence and uplift, intraplate stress, and inherited lithospheric structure in the late stage of the SE Carpathians evolution. Tectonics 26, TC4011, doi:10.1029/2006TC001951.

McDonough, W.F., Sun, S.-S., 1995. The composition of the Earth. Chemical Geology 120, 223-253.

McInnes, B.I.A., Grégoire, M., Binns, R.A., Herzig, P.M., Hannington, M.D., 2001. Hydrous metasomatism of oceanic sub-arc mantle, Lihir, Papua New Guinea: petrology and geochemistry of fuid-metasomatised mantle wedge xenoliths. Earth and Planetary Science Letters 188, 169-183.

Mercier, J.-C.C., Nicolas, A., 1975. Textures and fabrics of upper mantle peridotites as illustrated by xenoliths from basalts. Journal of Petrology 16, 454-487.

Merten, S., Matenco, L., Foeken, J.P.T., Stuart, F.M., Andriessen, P.A.M., 2010. From nappe stacking to out-of-sequence post-collisional deformations: Cretaceous to Quaternary exhumation history of the SE Carpathians assessed by low-temperature thermochronology. Tectonics 29, TC3013.

Molnár, K., Harangi, S., Lukács, R., Dunkl, I., Schmitt, A.K., Kiss, B., Garamhegyi, T., Seghedi, I., 2018. The onset of the volcanismin the Ciomadul Volcanic Dome Complex (Eastern Carpathians): eruption chronology and magma type variation. Journal of Volcanology and Geothermal Research 354, 39–56.

Moreira, M., Kunz, J., Allegre, C., 1998. Rare gas systematics in popping rock: Isotopic and elemental compositions in the upper mantle. Science 279, 1178–1181.

Moreira, M., 2013. Noble gas constraints on the origin and evolution of earth's volatiles. Geochemical Perspectives 2, 229–230.

Moreira, M., Rouchon, V., Muller, E., Noirez, S., 2018. The xenon isotopic signature of the mantle beneath Massif Central. Geochemical Perspective Letters 6, 28–32.

Niu, Y., Langmuir, C.H., Kinzler, R.J., 1997. The origin of abyssal peridotites: a new perspective. Earth and Planetary Science Letters 152, 251-265.

Niu, Y., 2004. Bulk-rock major and trace element compositions of abyssal peridotites: implications for mantle melting, melt extraction and post-melting processes beneath mid-ocean ridges. Journal of Petrology 45, 2423-2458.

Ntaflos, T., Bizimis, M., Abart, R., 2017. Mantle xenoliths from Szentbékálla, Balaton: Geochemical and petrological constraints on the evolution of the lithospheric mantle underneath Pannonian Basin, Hungary. Lithos 276, 30-44.

Oncescu, M.C., Burlacu, V., Anghel, M., Smalberger, V., 1984. Three-dimensional P-wave velocity image under the Carpathian arc. Tectonophysics 106, 305–319.

Parkinson, I.J., Arculus, R.J., Eggins, S.M., 2003. Peridotite xenoliths from Grenada, Lesser Antilles Island Arc. Contribution to Mineralogy and Petrology 146, 241–262.

Pécskay, Z., Lexa, J., Szakács, A., Seghedi, I., Balogh, K., Konečný, V., Zelenka, T., Kovacs, M., Póka, T., Fülöp, A., Márton, E., Panaiotu, C., Cvetković, V., 2006. Geochronology of Neogene–quaternary magmatism in the Carpathian arc and intra-Carpathian area: a review. Geol. Carpath. 57, 511–530.

Pilet, S., Ulmer, P., Villiger, S., 2010. Liquid line of descent of a basanitic liquid at 1.5 GPa: constraints on the formation of metasomatic veins. Contributions to Mineralogy and Petrology 159, 621–643.

Pouchou, J.L., Pichoir, F., 1991. Quantitative analysis of homogeneous or stratified microvolumes applied the model "PAP", in: Heinrich, K.F.J., Newbury, D.E. (Eds.), Electron Probe Quantification. Plenum, New York, London, pp. 31–35.

Popa, M., Radulian, M., Szakács, A., Seghedi, I., Zaharia, B., 2012. New seismic and tomography data in the southern part of the Harghita Mountains (Romania, Southeastern Carpathians): connection with recent volcanic activity. Pure and Applied Geophysics 169, 1557–1573.

Rizzo, A.L., Pelorosso, B., Coltorti, M., Ntaflos, T., Bonadiman, C., Matusiak-Małek, M., Italiano, F., Bergonzoni, G., 2018. Geochemistry of noble gases and CO_2 in fluid inclusions from lithospheric mantle beneath Wilcza Góra (Lower Silesia, Southwest Poland). Frontiers in Earth Sciences 6:215. doi: 10.3389/feart.2018.00215.

Roedder, E., 1984. Fluid inclusions reviews in mineralogy. Mineralogical Society of America 12, 644 doi: 10.1515/9781501508271.

Sarda, P., Staudacher, T., and Allègre, C.J. (1988). Neon isotopes in submarine basalts. Earth and Planetary Science Letters 91, 73–88.

Schmädicke, E., Gose, J., Will, T.M., 2011. Heterogeneous mantle underneath the North Atlantic: Evidence from water in orthopyroxene, mineral composition and equilibrium conditions of spinel peridotite from different locations at the Mid-Atlantic Ridge. Lithos 125, 308–320.

Scott, J.M., Liu, J., Pearson, D.G., Waight T.E., 2016. Mantle depletion and metasomatism recorded in orthopyroxene in highly depleted peridotites. Chemical Geology 441, 280-291.

Seghedi, I., Downes, H., Szakács, A., Mason, P.R.D., Thirlwall, M.F., Roşu, E., Pécskay, Z., Marton, E., Panaiotu, C., 2004. Neogene-Quaternary magmatism and geodynamics in the Carpathian–Pannonian region: a synthesis. Lithos 72, 117–146.

Seghedi, I., Matenco, L., Downes, H., Mason, P.R.D., Szakács, A., Pécskay, Z., 2011. Tectonic significance of changes in post-subduction Pliocene-Quaternary magmatism in the south east part of the Carpathian–Pannonian region. Tectonophysics 502, 146–157.

Seghedi, I., Downes, H., 2011. Geochemistry and tectonic development of Cenozoic magmatism in the Carpathian–Pannonian region. Gondwana Research, 20, 655–672.

Seghedi, I., Popa R-G., Panaiotu, C.G., Szakács, A., Pécskay, Z., 2016. Short-lived eruptive episodes during the construction of a Na-alkalic basaltic field (Perşani Mountains, SE Transylvania, Romania). Bulletin of Volcanology 78:69, DOI 10.1007/s00445-016-1063-y.

Seghedi, I., Besutiu, L., Mirea, V., Zlagnean, L., Răzvan-Gabriel, Popa, R-G, Szakács, A., Atanasiu, L., Pomeran, M., Vişan, M., 2019. Tectono-magmatic characteristics of post-collisional magmatism: Case study East Carpathians, Călimani-Gurghiu-Harghita volcanic range. Physics of the Earth and Planetary Interiors 293 (2019), 106270.

Seyler, M., Cannat, M.C., Mével, C., 2003. Evidence for major-element heterogeneity in the mantle source of abyssal peridotites from the Southwest Indian Ridge (52° to 68°E). Geochemistry Geophysics Geosystems 4, 9101, DOI:10.1029/2002GC000305.

Sorbadere F., Laurenz V., Frost D.J., Wenz M., Rosenthal A., McCammon C., Rivard C., 2018. The behaviour of ferric iron during partial melting of peridotite. Geochimica et Cosmochimica Acta 239, 235–254.

Szabó, Cs., Vaselli, O., Vannucci R., Bottazzi, P., Ottolini, L., Coradossi, N., Kubovics, I., 1995a. Ultramafic xenoliths from the Little Hungarian Plain (Western Hungary): a petrologic and geochemical study. Acta Vulcanologica 7, 249–263.

Szabó, C., Harangi, S., Vaselli, O., Downes, H., 1995b. Temperature and oxygen fugacity in peridotite xenoliths from the Carpathian-Pannonian Region. Acta Vulcanologica 7, 231-239.

Szakács, A., Seghedi, I., Pécskay, Z. 1993. Pecularities of South Harghita Mts. as terminal segment of the Carpathian Neogene to Quaternary volcanic chain. Revue Roumaine de Géologie 37, 21–36.

Takazawa, E., Frey, F.A., Shimizu, N., Obata, M., 2000. Whole rock compositional variation in an upper mantle peridotite (Horoman, Hokkaido, Japan): are they consistent with a partial melting process. Geochimica et Cosmochimica Acta 64, 695–716.

Taylor, W.R. 1998. An experimental test of some geothermometer and geobarometer formulations for upper mantle peridotites with application to the thermobarometry of fertile lherzolite and garnet websterite. Neues Jahrbuch für Mineralogie Abhandlungen 172, 381-408.

Trull, T.W., Kurz, M.D., 1993. Experimental measurements of ^{3}He and ^{4}He mobility in olivine and clinopyroxene at magmatic temperatures. Geochimica et Cosmochimica Acta 57, 1313–1324.

Vaselli, O., Downes, H., Thirlwall, M.F., Dobosi, G., Coradossi, N., Seghedi, I., Szakács, A., Vannucci, R., 1995. Ultramafic xenoliths in Plio-Pleistocene alkali basalts from the Eastern Transylvanian basin: depleted mantle enriched by vein metasomatism. Journal of Petrology 36, p.23-55.

Vaselli, O., Minissale, A., Tassi, F., Magro, G., Seghedi, I., Ioane, D., Szakács, A., 2002. A geochemical traverse across the Eastern Carpathians (Romania): constraints on the origin and evolution of the mineral waters and gas discharge. Chemical Geology 182, 637–654.

Zanetti, A., Vannucci, R., Oberti, R., Dobosi, G., 1995. Trace-element composition and crystal-chemistry of mantle amphiboles from the Carpatho-Pannonian region. Acta Vulcanologica 7, 265-276.

Ziberna, L., Klemme, S., Nimis, P., 2013. Garnet and spinel in fertile and depleted mantle: insights from thermodynamic modelling. Contribution to Mineralogy and Petrology 166, 411–421.

Witt-Eickschen, G., Harte, B., 1994. Distribution of trace elements between amphibole and clinopyroxene from mantle peridotites of the Eifel (western Germany): An ion-microprobe study. Chemical Geology 117, 235-250.

Wood, B.J., Virgo, D., 1989. Upper mantle oxidation state: ferric iron contents of lherzolite spinels by ^{57}Fe Mössbauer spectroscopy and resultant oxygen fugacities. Geochimica et Cosmochimica Acta 53, 1227–1291.

Workman, R.K., Hart, S.R., 2005. Major and trace element composition of the depleted MORB mantle (DMM). Earth and Planetary Science Letters 231, 53-72.

Yamamoto, J., Kaneoka, I., Nakai, S., Kagi, H., Prikhod'ko, V.S., Arai, S., 2004. Evidence for subduction-related components in the subcontinental mantle from low $^{3}He/^{4}He$ and $^{40}Ar/^{36}Ar$ ratio in mantle xenoliths from Far Eastern Russia. Chemical Geology 207, 237–259.

Yamamoto, J., Nishimura, K., Sugimoto, T., Takemura, K., Takahata, N., Sano, Y., 2009. Diffusive fractionation of noble gases in mantle with magma channels: origin of low He/Ar in mantle-derived rocks. Earth and Planetary Science Letters 280, 167–174.

Yoshikawa, M., Tamura, A., Arai, S., Kawamoto, T., Payot, B.D., Rivera, D.J., Bariso, E.B., Mirabueno, M.H.T., Okuno, M., Kobayashi, T., 2016. Aqueous fluids and sedimentary melts as agents for mantle wedge metasomatism, as inferred from peridotite xenoliths at Pinatubo and Iraya volcanoes, Luzon arc, Philippines. Lithos 262, 355-368.

FIGURE CAPTIONS (ONLINE COLOUR ONLY)

Fig. 1. Geological sketch of Pannonian Basin and volcanological map of Perşani Mountains in the Transylvanian Basin. C-G-H indicates the Călimani-Ghiurghiu-Harghita volcanic arc. The mantle xenolith sampling sites (LAG-BARC-TRE) correspond to loose pyroclastic deposits of La Gruiu volcanic center and Barc and Trestia creeks, respectively.

Fig. 2: Mg# vs Al_2O_3 (A) and TiO_2 (B) and Al_2O_3 vs Na_2O (C) of primary cpx in PMVF mantle xenoliths, divided by textural sub-groups. (a), anhydrous samples. Black square, PM cpx composition calculated through mass balance from Bulk Silicate Earth of McDonough and Sun (1995) and Johnson et al. (1990) modes. Thick line in (A), cpx melting model (Bonadiman and Coltorti, 2018). Small grey dots, PMVF cpx data from Vaselli et al. (1995). Black asterisks in (A) are cpx from Pacific arc mantle wedge xenoliths (Japan, Abe et al., 1998; Lihir, Mc Innes et al., 2001; Cascade Range, Brandon and Draper, 1996; Kamchatka, Kepezhinskas et al., 1996, Bryant and Yogodzinsky, 2007, Ishimaru et al., 2007, Ionov, 2010; Philippines, Arai et al., 2004).

Fig. 3. Mg# vs Al_2O_3 (A) and CaO (B) of opx in PMVF mantle xenoliths, divided by textural sub-groups. (a), anhydrous samples. Black square, PM opx composition calculated through mass balance from Bulk Silicate Earth of McDonough and Sun (1995) and Johnson et al. (1990) modes. Thick line, opx melting model according to Bonadiman and Coltorti (2018). Small grey dots, PMVF opx data from Vaselli et al. (1995). Black asterisks and violet crosses are respectively primary and secondary opx from Pacific arc mantle wedge xenoliths (Cascade Range, Brandon and Draper, 1996; Kamchatka, Kepezhinskas et al., 1996, Arai et al., 2003, Bryant and Yogodzinsky, 2007, Ishimaru et al., 2007, Ionov 2010, Ionov et al., 2013; Philippines, Arai et al., 2004, Yoshikawa et al., 2016).

Fig. 4. Mg# vs Al_2O_3 (A) and TiO_2 (B) of disseminated (amph-D) and vein (amph-V) amphiboles in PMVF mantle xenoliths, divided by textural sub-groups. Small grey dots, asterisks and squares are amphiboles in PMVF ultramafic xenoliths reported by Vaselli et al. (1995). Small black crosses (MXC), amphibole megacrysts found in Persani Mts pyroclastic deposits by Downes et al. (1995) and Zanetti et al. (1995).

Fig. 5. Mg# vs cr# of primary spinel in PMVF mantle xenoliths, divided by textural sub-groups. (a), anhydrous samples. Black square, PM spinel composition calculated through mass balance from Bulk Silicate Earth of McDonough and Sun (1995) and Johnson et al. (1990) modes. Small grey dots, PMVF spinel data from Vaselli et al. (1995).

Fig. 6. Chondrite normalized REE (A, C, E) and trace element (B, D, F) patterns of cpx in PMVF mantle xenoliths, divided in three Groups according to their geochemical features. Average patterns of disseminated amphibole associated to the different cpx Groups (black dotted lines) are also reported.

Fig. 7. Chondrite normalized REE (A, C, E) and trace element (B, D, F) patterns of opx in PMVF mantle xenoliths, divided in three Groups according to their geochemical features.

Fig. 8. Chondrite normalized REE (A, C, E) and trace element (B, D, F) patterns of amphibole in PMVF mantle xenoliths, divided in three Groups according to their geochemical features. Average patterns of the associated cpx (black dotted lines) are also reported. The pattern with asterisk symbol is LAG52 vein amphibole.

Fig. 9. Diagram of $^{21}Ne/^{22}Ne$ versus $^{20}Ne/^{22}Ne$ measured in fluid inclusions of PMVF xenoliths. Olivine abbreviated as "ol". The black dashed and dotted lines represent binary mixing between air ($^{21}Ne/^{22}Ne = 0.0290$ and $^{20}Ne/^{22}Ne = 9.8$) and i) MORB mantle as defined by Sarda et al. (1988) and Moreira et al. (1998) at $^{21}Ne/^{22}Ne = 0.06$ and $^{20}Ne/^{22}Ne = 12.5$; ii) CRUST as defined by Ballentine (1997) and references therein at $^{21}Ne/^{22}Ne = 0.6145$ (mean of 0.469-0.76) and $^{20}Ne/^{22}Ne = 0.3$; iii) SOLAR WIND as defined by Heber et al. (2009) at $^{21}Ne/^{22}Ne = 0.0328$ and $^{20}Ne/^{22}Ne = 13.8$. Data from other European localities are also reported (French Massif Central, Eifel, and Kapfenstein, Gautheron et al., 2005; Calatrava and Tallante, Martelli et al., 2011; Lower Silesia, Rizzo et al., 2018).

Fig. 10. Concentrations of a) ^{4}He and b) $^{40}Ar^*$ versus $^{3}He/^{4}He$ corrected for air contamination (Rc/Ra values). Olivine abbreviated as "ol". The blue bar indicates the range of $^{3}He/^{4}He$ ratios for a MORB-like mantle (8±1 Ra; Graham, 2002). The two diffusive fractionation paths are modeled based on the approach of Burnard et al. (1998), Burnard (2004) and Yamamoto et al. (2009), taking into account the diffusion coefficient (D) of ^{3}He, ^{4}He, and $^{40}Ar^*$ ($D_{3He}/D_{4He} = 1.15$ and $D_{4He}/D_{40Ar} = 3.16$ in solid mantle; Trull and Kurz, 1993; Burnard, 2004; Yamamoto et al., 2009). Starting and final conditions as well as further details on modelling are reported in the ESM4. Data from other European localities as in Fig. 9 caption.

Fig. 11. a) $^{3}He/^{36}Ar$ and b) ^{4}He (mol/g) versus $^{40}Ar/^{36}Ar$. Olivine abbreviated as "ol". The continuous and dashed turquoise lines represent binary mixing between air [$^{40}Ar/^{36}Ar$ = 295.5, $^{3}He/^{36}Ar = 2.3\times10^{-7}$ and $^{4}He = 1.1\times10^{-16}$ (arbitrarily fixed to fit data)] and MORB mantle as defined by Moreira et al. (1998), and Ballentine et al. (2005) at $^{40}Ar/^{36}Ar$ = 44,000, $^{3}He/^{36}Ar$ = 0.49 and $^{4}He = 1.0\times10^{-10}$ (arbitrarily fixed to fit data), considering $^{3}He/^{4}He$ = 8, $^{4}He/^{40}Ar^{*}$ = 1 and $^{4}He/^{40}Ar^{*}$ = 0.1. Data from other European localities as in Fig. 9 caption.

Fig. 12. Mg# vs A) ^{4}He, B) $^{40}Ar^{*}$, C) $^{4}He/^{40}Ar^{*}$, and D) $^{3}He/^{4}He$ corrected for air contamination (Rc/Ra values). MORB range is reported for $^{4}He/^{40}Ar^{*}$ and $^{3}He/^{4}He$ corrected for air contamination (Rc/Ra values). The expected trend lines for partial melting or refertilisation processes are reported.

Fig. 13. Discrimination diagrams for amphibole geodynamic affinity (Coltorti et al., 2007b). I-amph, Intraplate amphibole; S-amph, Subductive amphibole. Amph-V and MXC are the composition of PMVF vein amphibole and Perşani Mts. megacrysts, respectively, as reported by Zanetti et al. (1995).

Fig. 14. Average Chondrite-normalized REE patterns of PMVF disseminated amphibole (symbols as in Fig. 8, abbreviations as in Fig. 4) and LAG52 vein amphibole compared to literature data of PMVF vein amphibole (pink shaded field, Zanetti et al., 1995; Vaselli et al., 1995; Chalot-Prat and Boullier, 1997) and Perşani Mts. megacrysts (MXC, Downes et al., 1995; Zanetti et al., 1995). Red and cyan triangles are megacryst compositions representing frozen alkaline melts at open and closed system conditions, according to Zanetti et al. (1995).

Fig. 15. Chondrite-normalized REE patterns of the calculated melt in equilibrium with LAG52 amphibole vein (yellow dots) and of the calculated cpx (red diamonds) in equilibrium with this

melt. Frozen alkaline metasomatic melt according to Zanetti et al. (1995) (cyan triangles), composition of cpx in a PMVF clinopyroxenite (pink diamonds, Chalot-Prat and Boullier, 1997), average PMVF cpx (symbols as in Fig. 6) and Perşani Mts. lavas (grey field, Downes et al., 1995; Harangi et al., 2013) are also reported.

Table 1: Petrographic description, main average petrological data, temperature-pressure-fO_2 estimates and modes for the analyzed PMVF mantle xenoliths. See text for further explanations and model references.

SAMPLE	GROUP	Sub-group	ROCK TYPE	fo	cr#	T (°C)* BK	T (° Tay
BARQ 4	Protogranular	*Pr s.s.*	Lh	89.9 ±0.12	8.93 ±0.09	1056 ±5.9	1009
LAG 2	Protogranular	*Pr s.s.*	Lh(a)	90.5 ±0.03	13 ±0.57	1048 ±0.7	1003
LAG 21	Protogranular	*Pr s.s.*	Lh(a)	89.7 ±0.17	12 ±2.12	1018 ±12	989
LAG 24	Protogranular	*Pr s.s.*	Lh(a)	89.8 ±0.11	9.48 ±0.22	1036 ±6.6	984 ±
LAG 51	Protogranular	*Pr s.s.*	Lh(a)	90.3 ±0.31	9.91 ±0.42	1023 ±14	997
LAG 52	Protogranular	*Pr s.s.*	Lh(a)	89.3 ±0.20	15.8 ±1.50	992 ±6.7	978
TRE 2	Protogranular	*Pr s.s.*	Lh(a)	90.7 ±0.07	15.5 ±0.49	1008 ±2.3	980 ±
LAG 1	Protogranular	*Pr srg*	Lh(a)	89.5 ±0.05	9.73 ±0.22	1010 ±3.5	983 ±
TRE 3	Porphyroclastic	*Po lrg*	Lh(a)	90.0 ±0.04	10.9 ±0.06	970 ±0.7	950 ±
TRE 1	Porphyroclastic	*Po s.s.*	Hz	91.5 ±0.27	31.2 ±2.49	897 ±6.2	890 ±
TRE 4 Pd	Porphyroclastic	*Po s.s.*	Lh(a)	90.0 ±0.13	10.5 ±1.10	843 ±12	858
TRE 4 Px	Porphyroclastic	*Po s.s*	Wb(a)		6.64	778 ±7.4	793 ±

(a) contains amphibole

* temperatures calculated at 2.0 GPa

§ pressure estimated using BK temperature at 2.0 Gpa

BK and Taylor stands for Brey and Köhler (1990) and Taylor (1998) thermometers, respectively

± indicates standard deviations on about 4 mineral pairs for the geothermomethers and single minerals for the geobaromether

Sample	BARQ 4	LAG21	LAG24	LAG51	LAG52	TRE2	LAG1	TRE1	TRE 4 Pd	TRE 4 Px
Rock type	Lh	Lh(a)	Lh(a)	Lh(a)	Lh(a)	Lh(a)	Lh(a)	Hz	Lh(a)	Wb(a)
Sub-	*Pr s.s.*	*Pr s.s.*	*Pr s.s.*	*Pr s.s.*	*Pr s.s.*	*Pr s.s.*	*Pr srg*	*Po s.s.*	*Po*	

Table 2. Representative trace element analyses of cpx in PMVF mantle xenoliths, divided by textural sub-groups. Ti values from EMP. Empty cells are bdl or undetected values.

group																*s.s.*	
Li	1.56	1.26	1.67	1.69	1.55	1.45	0.75	1.88	1.71	1.79			1.96	1.29			2.97	4.86
Cs		0.05		0.24														0.02
Rb				0.29	0.05					0.04				0.03			0.02	0.05
Ba	0.34	0.14	0.71	0.12		0.06				0.20			0.14				0.43	0.19
Th	0.28	0.35	0.23	0.24	0.04	0.04	1.08	0.42	0.41	0.70			0.35	0.09	1.39	0.74	0.08	0.32
U	0.10	0.09	0.30	0.28	0.03		0.82	0.10	0.09	0.06			0.04	0.05			0.01	0.12
Nb	0.15	0.06	0.06	0.17	0.07	0.10	1.06	0.03	0.38				0.05	0.08				0.04
Ta		0.01	0.02	0.01				0.02					0.01	0.01				0.01
La	2.23	1.63	1.08	1.22	1.17	1.14	4.24	2.74	5.50	6.13	1.08	0.91	1.54	1.13	4.05	2.58	0.94	1.73
Ce	5.32	4.06	3.86	3.96	4.21	4.00	8.35	9.19	9.17	9.31	2.37	2.55	3.86	3.65	4.47	3.47	5.32	3.38
Pb	0.20		0.22	0.31	0.13		0.44	0.17	0.54	0.38			0.15		0.61	0.55	0.31	0.81
Pr	0.62	0.74	0.88	0.80	0.71	0.79	1.22	1.17	1.08	1.36	0.39	0.41	0.57	0.65	0.45	0.38	0.59	0.62
Sr	79.2	74.0	56.8	58.8	69.7	66.3	82.8	85.1	62.8	54.5	24.8	25.1	82.1	79.4	58.6	53.3	44.6	51.3
Nd	3.82	4.63	4.77	4.52	4.74	4.91	8.62	5.66	6.04	6.11	2.76	2.52	3.51	3.19	2.16	1.91	3.52	3.92
Zr	42.3	45.3	40.8	40.9	41.6	40.4	41.9	28.1	46.0	41.1	21.2	16.0	21.2	16.5	19.1	14.3	21.6	24.8
Hf	1.18	1.06	1.73	1.86	1.17	1.03	0.99	0.83	1.39	1.15			0.79	0.75			0.59	0.71
Sm	1.57	2.00	2.02	2.02	1.87	1.85	2.39	2.11	2.11	1.46			1.23	1.18	1.07	0.92	1.46	1.77
Eu	0.80	0.96	0.93	1.12	0.99	0.70	1.14	0.76	0.76	0.70	0.49	0.54	0.42	0.55	0.35	0.38	0.57	0.69
Ti	3780	4187	3717	2964	3646	3546	3128	2213	1872	2411	1676	1730	1866	1893	906	947	3383	2098
Gd	2.43	3.26	3.20	3.62	3.40	2.68	2.59	2.50	2.50	1.84	2.67	1.91	1.61	1.35	1.87	1.34	2.48	2.32
Tb	0.49	0.58	0.63	0.77	0.60	0.50	0.42	0.43	0.59	0.42			0.41	0.30			0.47	0.45
Dy	4.49	4.21	4.10	3.93	3.84	3.47	3.80	2.71	3.61	3.46	3.36	2.35	2.48	1.70	2.15	1.64	3.37	3.20
Y	21.2	22.7	21.3	20.1	20.3	23.3	19.7	12.7	18.7	15.8	23.0	15.5	13.0	9.13	13.7	10.9	19.1	17.6
Ho	0.88	0.89	0.98	1.09	0.87	0.79	0.80	0.60	0.80	0.57	0.81	0.53	0.55	0.34	0.49	0.35	0.72	0.71
Er	2.20	2.54	2.54	2.70	2.27	2.15	2.27	1.91	2.46	2.04	2.46	1.62	1.48	1.10	1.38	0.97	1.73	1.96
Tm	0.38	0.43	0.36	0.37	0.33	0.33	0.25	0.24	0.34	0.28			0.22	0.19			0.28	0.30
Yb	2.78	2.74	2.10	2.13	2.17	2.24	2.14	1.45	3.18	1.76	2.04	1.62	1.50	1.37	1.52	1.00	1.78	1.87
Lu	0.40	0.40	0.41	0.30	0.32	0.30	0.26	0.20	0.39	0.28			0.23	0.18	0.24	0.18	0.28	0.26

Sample	BARQ4		LAG21		LAG24		LAG51		LAG52		TRE2		LAG1	
Rock type	Lh		Lh(a)		Lh(a)		Lh(a)		Lh(a)		Lh(a)		Lh(a)	
Sub-group	*Pr s.s.*		*Pr s.s.*		*Pr s.s.*		*Pr s.s.*		*Pr s.s.*		*Pr s.s.*		*Pr srg*	
Li	1.08	0.99	1.43	1.72	1.21	1.45	1.80		0.01	3.53			2.13	1.42
Cs										0.02				
Rb			0.06					0.07	0.25	0.23		0.21		0.03
Ba			0.25	0.08				0.53	0.02			1.53	0.61	0.65
Th	0.02	0.01	0.00	0.01		0.01	0.08		0.23		0.09	0.06	0.01	
U		0.00		0.04					0.04	1.14	0.01		0.01	0.01
Nb	0.04		0.02		0.01		0.17	0.08	2.63	0.01	0.22	0.35	0.19	0.12
Ta									0.12	0.01			0.00	0.00
La		0.01	0.02	0.02	0.01		0.06	0.02	0.05	0.01	0.04	0.13	0.03	0.03
Ce	0.02	0.02	0.03	0.08	0.02	0.13	0.14	0.05	0.01	0.05	0.05	0.20	0.05	0.12
Pb	0.10	0.13	0.06		0.05	0.05	0.71		0.46	0.62			0.17	
Pr	0.01		0.01	0.01	0.01	0.03	0.02			0.01	0.01	0.02	0.01	0.01
Sr	0.17	0.15	0.79	0.80	0.22	0.98	1.07	0.34	0.04	0.12	0.27	1.43	0.90	
Nd	0.04	0.04	0.04	0.05		0.18	0.17	0.08	0.26		0.05	0.09	0.08	0.10
Zr	2.78	2.54	1.94	2.11	1.62	2.38	2.34		1.58	1.72			1.66	1.41
Hf	0.11	0.08	0.06	0.04		0.10			0.06	0.05			0.05	0.03
Sm		0.03		0.05			0.06	0.05		0.05	0.04	0.04	0.03	0.03
Eu	0.02	0.02		0.03		0.04	0.03	0.04	0.07	0.02	0.02	0.02	0.02	0.01
Ti	756	791	542	583	642	809	684	635	746	576	511	501	421	551
Gd	0.06	0.03				0.13	0.11		0.16		0.11	0.10	0.09	
Tb	0.02	0.03	0.02	0.03	0.01	0.03	0.03		0.02	0.01			0.01	0.01
Dy	0.21	0.23	0.11	0.17	0.10	0.25	0.23	0.12	0.18	0.09	0.18		0.12	0.08
Y	1.57	1.52	1.02	1.12	1.11	1.59	1.61	0.99	1.35	0.85	1.43	1.07	0.94	0.70
Ho	0.06	0.06	0.03	0.03	0.04	0.06	0.07	0.03	0.05	0.04	0.06	0.05	0.04	0.03
Er	0.34	0.21		0.16	0.13	0.20	0.38	0.25	0.25	0.23	0.32	0.22	0.16	0.17
Tm	0.06	0.04	0.03	0.03	0.03	0.04			0.07	0.04			0.03	
Yb	0.55	0.36	0.20	0.28	0.26	0.33	0.47	0.35	0.47	0.26	0.48	0.29	0.25	0.21
Lu	0.09	0.08	0.04	0.05	0.04	0.06	0.07	0.04	0.09	0.03	0.07	0.06	0.05	0.04

Table 3. Representative trace element analyses of opx in PMVF mantle xenoliths, divided by textural sub-groups. Ti values from EMP. Empty cells are bdl or undetected values.

Table 4. Representative trace element analyses of amphibole in PMVF mantle xenoliths, divided by textural

Sample	LAG21		LAG24		LAG51		LAG52			TRE2	
Rock type	Lh(a)		Lh(a)		Lh(a)		Lh(a)			Lh(a)	
Sub-group	*Pr s.s.*		*Pr s.s.*		*Pr s.s.*		*Pr s.s.*			*Pr s.s.*	
phase	amph-D	amph-D	amph-D	amph-D	amph-D	amph-D	amph-D	amph-D	amph-V	amph-D	amph-D
Li	2.07	2.03	0.52	0.96	2.54	2.00	0.41	0.84	0.56		
Cs		0.03				0.06	0.05	0.19	0.03		
Rb	0.43	0.33	0.37	0.56		1.86	4.87	7.71	8.05		
Ba	26.6	10.6	8.0	20.8	22.9	64.2	20.0	69.0	228	1.78	3.77
Th	0.02	0.02		0.04	0.44	0.29	0.38	0.53	0.27	0.32	0.39
U	0.02		0.03		0.12	0.20	0.12	0.18	0.11	0.03	
Nb	1.73	1.44	2.98	2.73	2.04	2.63	12.9	16.6	63.1	1.92	2.29
Ta	0.06	0.08	0.18	0.21	0.15	0.13	0.28	0.57	2.59		
La	1.15	1.19	1.37	1.15	4.86	4.10	3.79	7.21	12.01	0.96	1.58
Ce	4.08	4.07	4.30	4.52	9.92	10.6	14.0	15.7	35.6	1.68	2.65
Pb	0.51	0.44	0.14	0.22	1.07	0.96	0.95	1.13	1.36		0.76
Pr	0.69	0.75	0.84	0.81	1.32	1.46	1.58	1.83	4.84	0.26	0.37
Sr	163	161	199	200	240	244	240	217	400	45.3	68.0
Nd	5.32	4.16	5.49	5.44	6.97	6.31	6.15	8.45	24.3	1.73	2.62
Zr	40.8	36.7	33.7	35.1	36.0	27.1	57.6	51.2	76.1		22.3
Hf	0.51	0.79	0.85	1.22	0.93	0.70	1.22	1.50	3.03		
Sm	2.28	1.78	2.25	1.76	1.74	1.51	1.82	2.61	5.71	0.95	1.11
Eu	0.81	1.01	0.90	0.87	0.92		0.60	0.88	1.93	0.36	0.46
Ti	10595	10540	13778	13667	8557	8833	6152	6636	10343	6262	7975
Gd	3.78	2.30	3.16	2.83	1.48	1.78	1.88	2.74		2.01	2.47
Tb	0.48	0.56	0.58	0.50	0.63	0.43	0.48	0.54	0.87		
Dy	3.09	3.72	3.90	3.76	3.61	2.52	2.62	2.59	4.62	2.85	3.11
Y	23.2	24.5	20.7	21.5	21.8	14.7	15.6	15.4	19.5	18.0	24.0
Ho	0.72	0.74	0.79	0.85	0.89	0.59	0.65	0.63	0.72	0.66	0.84
Er	2.24	2.14	2.30	2.19	2.61	1.72	1.92	2.03	1.86	1.91	2.63
Tm	0.37	0.38	0.34	0.37	0.38	0.28	0.24	0.24	0.24		
Yb	2.73	2.41	2.21	2.34	2.55	2.03	1.80	1.38	1.46	2.09	2.73
Lu	0.28	0.25	0.31	0.33	0.37	0.23	0.17	0.22	0.23	0.30	0.38

sub-groups. Ti values from EMP. Empty cells are bdl or undetected values. amph-D, disseminated amphibole; amph-V, vein amphibole.

Table 5. Geochemistry of fluid inclusions hosted in minerals forming mantle xenoliths from PMVF. Ol, olivine; Cpx, clinopyroxene; Opx, orthopyroxene. n.a. indicates not available, n.m. stands for not measured.

Sample	Mineral	weight (g)	^{4}He mol/g	^{20}Ne mol/g	^{21}Ne mol/g	^{22}Ne mol/g	^{40}Ar mol/g	^{36}Ar mol/g	^{40}Ar* mol/g	^{4}He/^{22}Ne	^{4}He/^{40}Ar*	R/Ra	Rc/Ra	Err Rc/Ra +/-	^{40}Ar/^{36}Ar	Err (%)	^{38}Ar/^{36}Ar	Err (%)	^{20}Ne/^{22}Ne	Err 20/22 +/-	^{21}Ne/^{22}Ne	Err 21/22 +/-	^{3}He	^{3}He/^{4}Ar
BARQ4	Ol	0.7025	3.50E-14	6.91E-15	1.89E-17	6.63E-15	2.65E-13	8.12E-16	2.46E-14	5.1	1.42	4.90	5.18	0.323	325.8	0.32	0.19334	0.19	10.02	0.03	0.0317	0.00046	2.52E-19	3.11E-04
LAG2	Ol	0.70675	2.07E-14	5.81E-16	4.12E-19	5.57E-16	4.88E-13	1.63E-15	7.51E-15	35.7	2.76	2.07	2.09	0.258	300.1	0.18	0.18869	0.19	n.m.	n.m.	n.m.	n.m.	6.02E-20	3.70E-05
LAG21	Ol	0.7169	1.34E-14	2.03E-14	5.82E-17	1.95E-14	1.80E-12	6.09E-15	n.a.	0.7	n.a.	n.m.	n.m.	n.m.	295.6	0.06	0.18742	0.19	10.04	0.02	0.0303	0.00025	n.a.	n.a.
LAG24	Ol	1.16645	4.18E-14	1.00E-15	2.93E-18	9.45E-16	8.62E-13	2.90E-15	n.a.	41.7	n.a.	1.51	1.51	0.114	297.4	0.06	0.18667	0.19	9.93	0.05	0.0291	0.00089	8.78E-20	n.a.
LAG51	Ol	0.72951	1.58E-14	7.25E-15	2.01E-17	6.95E-15	n.m.	n.m.	n.a.	2.2	n.a.	n.m.	n.m.	n.m.	n.m.	n.m.	n.m.	n.m.	9.91	0.03	0.0314	0.00044	n.a.	n.a.
LAG52	Ol	0.72483	9.43E-14	5.04E-15	1.36E-17	4.84E-15	2.06E-12	6.83E-15	4.23E-14	18.7	2.23	5.32	5.40	0.209	301.7	0.05	0.18733	0.19	9.93	0.04	0.0327	0.00065	7.08E-19	1.04E-04
TRE2	Ol	1.27606	2.76E-14	4.54E-15	1.35E-17	4.28E-15	1.81E-12	6.29E-15	n.a.	6.1	n.a.	5.64	5.92	0.144	287.8	0.00	0.18258	0.18	n.m.	n.m.	n.m.	n.m.	2.27E-19	n.a.
LAG1	Ol	0.71426	3.31E-14	1.47E-14	4.22E-17	1.41E-14	2.07E-12	6.92E-15	n.a.	2.3	n.a.	2.48	2.77	0.284	298.5	0.05	0.18843	0.19	10.03	0.02	0.0308	0.00033	1.28E-19	1.84E-05
TRE3	Ol	1.10012	5.71E-14	5.76E-14	1.68E-16	5.43E-14	9.09E-12	3.18E-14	n.a.	1.0	n.a.	2.26	2.98	0.081	286.1	0.00	0.18235	0.18	n.m.	n.m.	n.m.	n.m.	2.37E-19	n.a.
TRE1	Ol	1.19089	6.02E-14	5.18E-14	1.52E-16	4.88E-14	2.42E-11	8.20E-14	n.a.	1.2	n.a.	3.78	4.93	0.091	295.1	0.00	0.18551	0.19	9.96	0.01	0.0292	0.00018	4.12E-19	n.a.
TRE4 Pd	Ol	0.82059	2.46E-14	1.21E-15	3.47E-18	1.16E-15	1.29E-12	4.33E-15	n.a.	20.4	n.a.	3.24	3.28	0.266	298.0	0.00	0.18741	0.19	9.82	0.09	0.0283	0.00110	1.12E-19	2.59E-05
BARQ4	Opx	0.68572	2.17E-13	1.92E-15	5.79E-18	1.84E-15	3.63E-13	4.87E-16	2.19E-13	112.8	0.99	6.27	6.29	0.122	744.0	0.1[illegible]	0.[illegible]95	0.21	9.91	0.08	0.0299	0.00129	1.90E-18	3.89E-03
LAG2	Opx	0.70223	6.70E-13	7.18E-15	2.12E-17	6.89E-15	9.84E-13	1.41E-15	5.68E-13	93.3	1.18	5.78	5.79	0.074	699.2	0.22	0.[illegible]06	0.20	9.91	0.03	0.0292	0.00049	5.40E-18	3.83E-03
LAG21	Opx	0.91336	1.20E-13	1.08E-14	3.07E-17	1.04E-14	7.44E-13	2.13E-15	1.16E-13	11.1	1.04	5.70	5.84	0.136	35[illegible]	0.14	0.18744	0.19	9.96	0.02	0.0307	0.00040	9.76E-19	4.59E-04
LAG24	Opx	0.99661	3.25E-13	1.66E-16	5.05E-19	1.56E-16	5.25E-13	5.97E-16	3.49E-13	1959.8	0.93	5.78	5.78	0.084	979.5	0.[illegible]0	0.20017	0.20	n.m.	n.m.	n.m.	n.m.	2.61E-18	n.a.
LAG51	Opx	0.70574	5.15E-13	3.00E-15	6.96E-18	2.88E-15	1.13E-12	1.50E-15	6.86E-13	171.5	0.75	5.75	5.76	0.088	752.8	0.20	0.18779	0.19	10.06	0.05	0.0342	0.00109	4.12E-18	2.75E-03
LAG52	Opx	0.62378	1.54E-12	7.75E-15	2.33E-17	7.44E-15	1.89E-12	2.15E-15	1.25E-12	199.1	1.23	6.08	6.09	0.[illegible]	87[illegible]5	0.13	0.18718	0.19	9.98	0.03	0.0300	0.00049	1.31E-17	6.07E-03
TRE2	Opx	1.02899	2.95E-13	5.80E-16	1.82E-18	5.46E-16	1.09E-12	2.96E-15	2.13E-13	508.8	1.38	6.80	6.80	0.083	867.5	0.00	0.18534	0.18	n.m.	n.m.	n.m.	n.m.	2.79E-18	n.a.
LAG1	Opx	0.45897	1.49E-13	6.95E-16	1.47E-18	6.66E-16	3.66E-13	8.27E-16	1.21E-13	215.2	1.23	5.77	5.78	0.182	442.4	0.56	0.18739	0.19	9.83	0.23	n.m.	n.m.	1.20E-18	1.45E-03
TRE3	Opx	1.11913	1.39E-13	5.94E-15	1.72E-17	5.60E-15	3.12E-12	8.89E-15	4.95E-13	23.5	0.28	5.35	5.41	0.081	351.1	0.06	0.18315	0.18	10.03	0.02	0.0291	0.00039	1.05E-18	n.a.
TRE1	Opx	1.0626	3.94E-13	2.79E-16	1.03E-18	2.63E-16	4.90E-13	1.01E-15	1.90E-13	1408.5	2.07	6.00	6.02	0.081	483.1	0.00	0.18096	0.18	n.m.	n.m.	n.m.	n.m.	3.61E-18	n.a.
TRE4 Pd	Opx	0.14468	3.64E-13	6.60E-15	1.95E-17	6.33E-15	6.85E-13	1.20E-15	3.32E-13	55.1	1.10	5.73	5.76	0.144	573.0	0.68	0.23387	0.23	10.01	0.06	0.0296	0.00130	2.91E-18	2.44E-03
BARQ4	Cpx	0.2825	3.57E-13	4.20E-16	6.68E-18	3.98E-16	7.39E-13	1.51E-15	2.92E-13	849.9	1.22	5.[illegible]8	5.88	0.132	488.9	0.64	0.19450	0.19	n.m.	n.m.	n.m.	n.m.	2.92E-18	1.93E-03
LAG2	Cpx	0.53856	1.18E-12	2.48E-15	8.43E-18	2.35E-15	1.42E-12	9.13E-16	1.15E-12	477.4	1.01	5.98	5.98	0.076	1551.2	0.45	0.17961	0.18	10.12	0.07	0.0346	0.00081	9.82E-18	1.08E-02
LAG21	Cpx	0.29793	3.23E-13	4.51E-15	1.29E-17	4.30E-15	7.48E-13	7.75E-16	5.19E-13	71.6	0.[illegible]	6.10	6.13	0.130	965.6	0.66	0.21744	0.22	n.m.	n.m.	0.0290	0.00094	2.75E-18	3.55E-03
LAG24	Cpx	0.50807	2.25E-13	1.61E-16	3.32E-19	1.52E-16	4.62E-13	4.33E-16	3.34E-13	1393.[illegible]	0.67	5.86	5.86	0.110	1067.4	0.57	0.20185	0.20	n.m.	n.m.	n.m.	n.m.	1.83E-18	n.a.
LAG51	Cpx	0.46538	5.73E-13	5.51E-15	1.65E-17	5.27E-15	1.14E-12	6.08E-16	9.56E-13	104.[illegible]0	0.60	5.73	5.74	0.091	1867.3	0.47	0.20754	0.21	10.03	0.04	0.0301	0.00054	4.58E-18	7.52E-03
LAG52	Cpx	0.32425	1.36E-12	9.93E-16	4.62E-18	9.43E-16	2.03E-12	1.65E-15	1.5[illegible]E-12	13[illegible].2	0.88	5.90	5.90	0.066	1230.9	0.46	0.17870	0.18	n.m.	n.m.	n.m.	n.m.	1.12E-17	6.77E-03
TRE2	Cpx	0.52521	8.36E-13	2.87E-15	8.56E-18	2.70E-15	2.52E-12	6.29E-15	6.[illegible]61E-13	[illegible]8	1.27	6.82	6.82	0.074	400.6	0.07	0.18527	0.19	9.89	0.06	0.0296	0.00082	7.93E-18	n.a.
LAG1	Cpx	0.50514	1.67E-13	2.09E-15	1.18E-17	1.98E-15	2.77E-13	4.42[illegible]	1.47E-13	79.8	1.14	5.48	5.50	0.144	627.6	1.20	0.19236	0.19	9.96	0.07	n.m.	n.m.	1.27E-18	2.88E-03
TRE3	Cpx	0.4656	1.27E-13	1.53E-14	4.37E-17	1.44E-14	5.05E-12	1.[illegible]3E-15	3.[illegible]5E-13	8.3	0.34	5.10	5.27	0.123	319.0	0.05	0.18293	0.18	n.m.	n.m.	n.m.	n.m.	9.33E-19	n.a.
TRE1	Cpx	0.53353	9.63E-13	5.69E-15	1.71E-17	5.37E-15	3.55E-12	1.07[illegible]	3.99E-13	169.1	2.41	6.50	6.51	0.072	332.9	0.06	0.18460	0.18	9.92	0.03	0.0298	0.00050	8.72E-18	n.a.
TRE4 Pd	Cpx	0.0718	1.86E-13	4.35E-15	4.61E-17	4.13E-15	9.1[illegible]E-13	2.85[illegible]E-15	7.43E-14	42.8	2.51	2.16	2.17	0.217	321.6	1.14	0.16051	0.16	n.m.	n.m.	n.m.	n.m.	5.63E-19	1.98E-04

^{40}Ar* was not calculated in those samples where ^{40}Ar/^{36}Ar was available but lower than 300.

HIGHLIGHTS

- Two different kinds of metasomatism in Eastern Transylvania lithospheric mantle
- The mantle wedge was refertilized by a calc-alkaline melt
- Refertilization was followed by alkaline metasomatism, forming amphibole veins
- He-Ne-Ar systematics indicate SCLM refertilization by subduction-related melts

Declaration of interests

☒ The authors declare that they have no known competing financial interests or personal relationships that could have appeared to influence the work reported in this paper.

☐The authors declare the following financial interests/personal relationships which may be considered as potential competing interests:

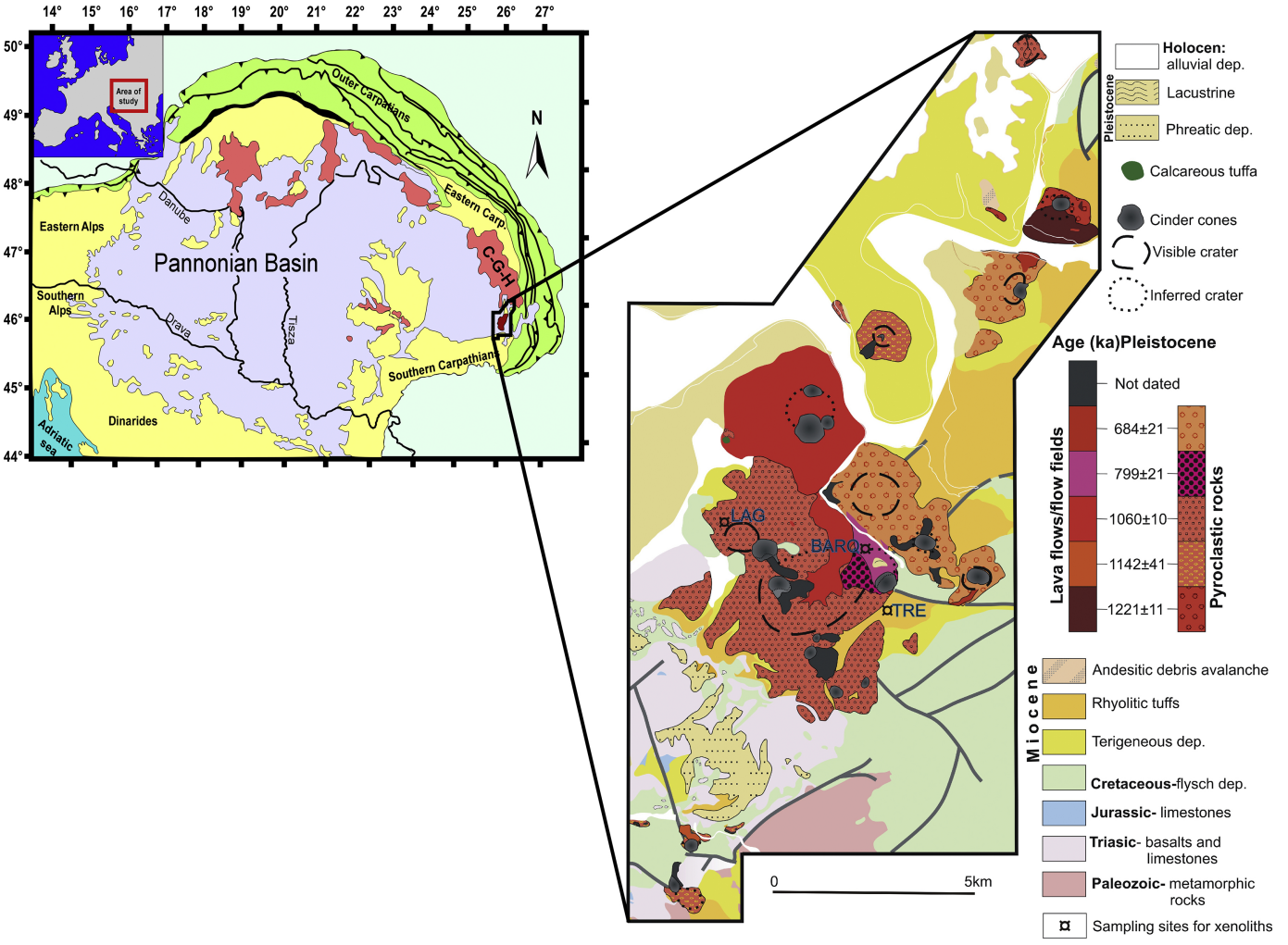
14° 15° 16° 17° 18° 19° 20° 21° 22° 23° 24° 25° 26° 27°
50° 49° 48° 47° 46° 45° 44°
Area of study
Outer Carpatians
N
Danube
Eastern Alps
Pannonian Basin
Eastern Carp.
C-G-H
Southern Alps
Drava
Tisza
Southern Carpathians
Dinarides
Adriatic sea
LAG
BARO
TRE
0
5km
Holocen:
alluvial dep.
Pleistocene
Lacustrine
Phreatic dep.
Calcareous tuffa
Cinder cones
Visible crater
Inferred crater
Age (ka)Pleistocene
Not dated
684±21
799±21
1060±10
1142±41
1221±11
Lava flows/flow fields
Pyroclastic rocks
Miocene
Andesitic debris avalanche
Rhyolitic tuffs
Terigeneous dep.
Cretaceous-flysch dep.
Jurassic- limestones
Triasic- basalts and limestones
Paleozoic- metamorphic rocks
Sampling sites for xenoliths

Figure 1

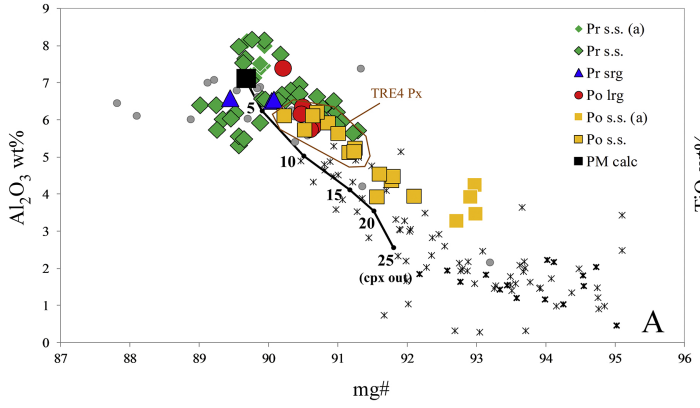
Pr s.s. (a)
Pr s.s.
Pr srg
Po lrg
Po s.s. (a)
Po s.s.
PM calc
TRE4 Px
5
10
15
20
25
(cpx out)
A
Al2O3 wt%
mg#

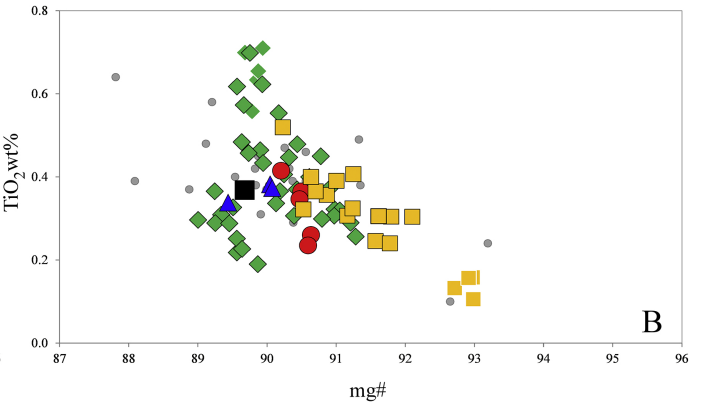
B
TiO2 wt%
mg#

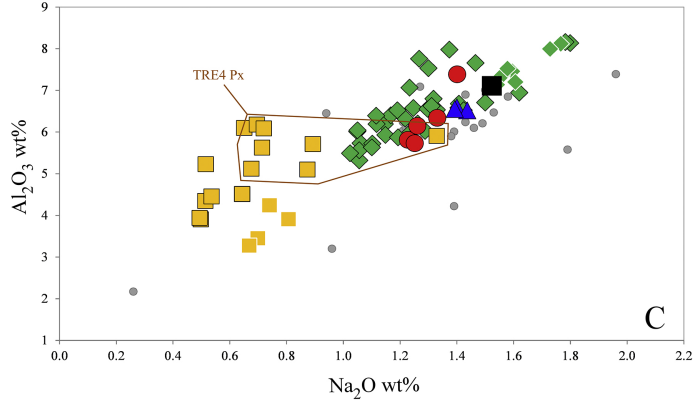
TRE4 Px
C
Al2O3 wt%
Na2O wt%

Figure 2

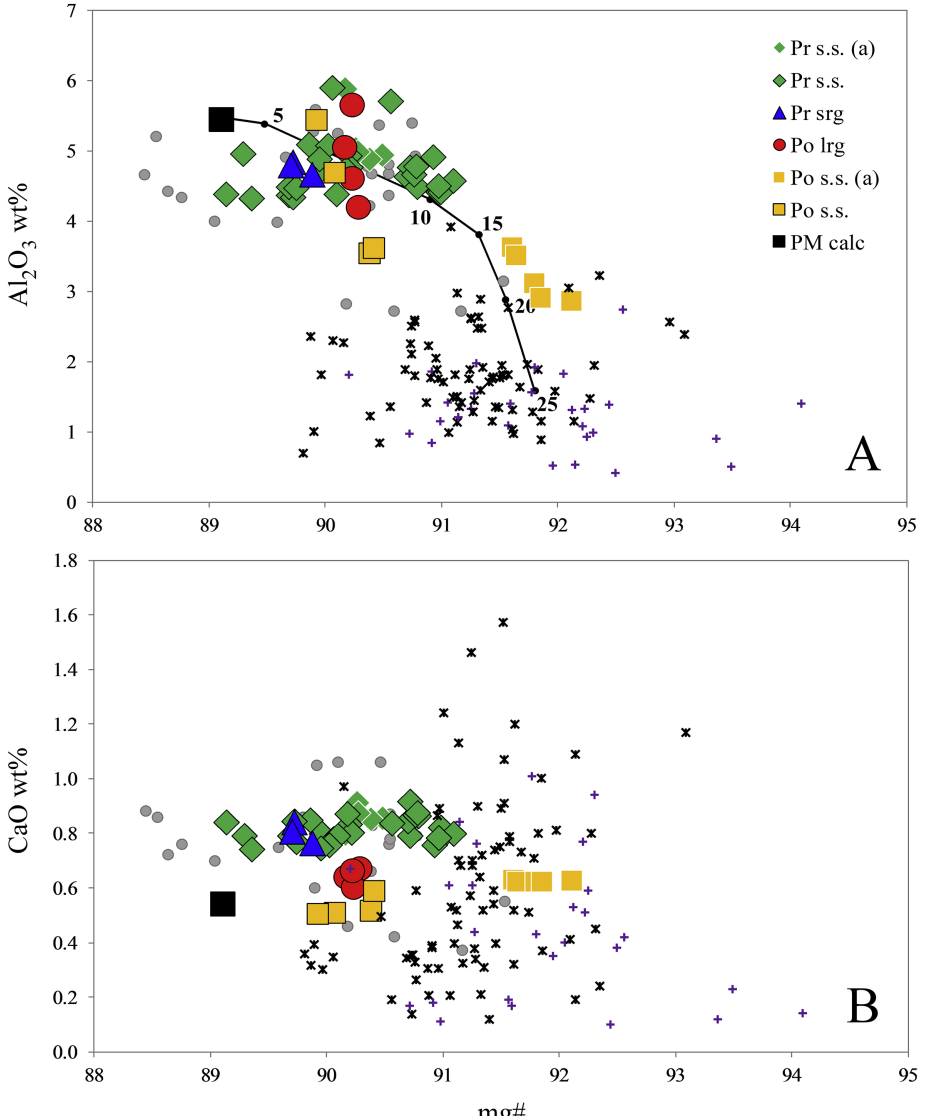
Pr s.s. (a)
Pr s.s.
Pr srg
Po lrg
Po s.s. (a)
Po s.s.
PM calc
5
10
15
20
25
Al_2O_3 wt%
A
CaO wt%
B
mg#

Figure 3

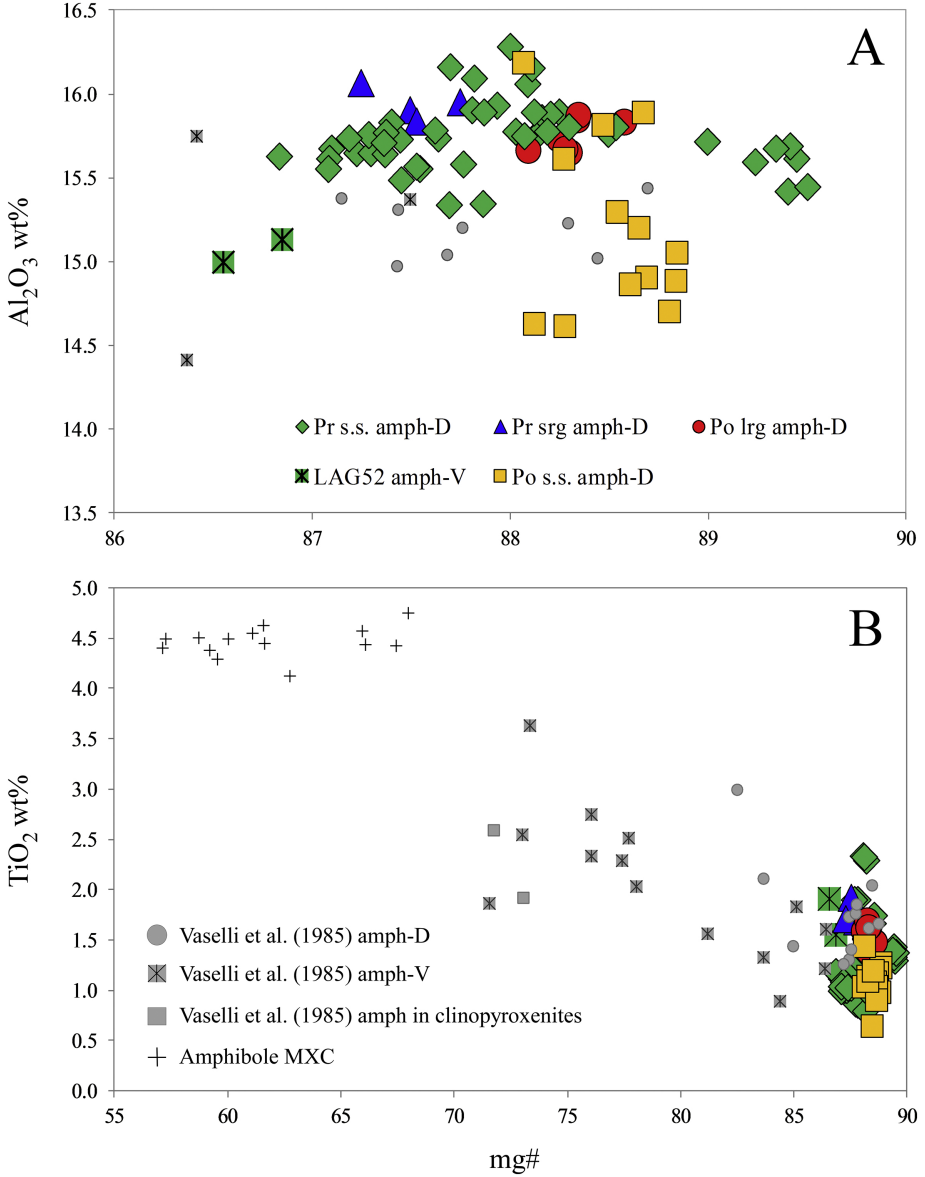
A
Al_2O_3 wt%
16.5
16.0
15.5
15.0
14.5
14.0
13.5
86
87
88
89
90
Pr s.s. amph-D
Pr srg amph-D
Po lrg amph-D
LAG52 amph-V
Po s.s. amph-D
B
TiO_2 wt%
5.0
4.5
4.0
3.5
3.0
2.5
2.0
1.5
1.0
0.5
0.0
55
60
65
70
75
80
85
90
mg#
Vaselli et al. (1985) amph-D
Vaselli et al. (1985) amph-V
Vaselli et al. (1985) amph in clinopyroxenites
Amphibole MXC

Figure 4

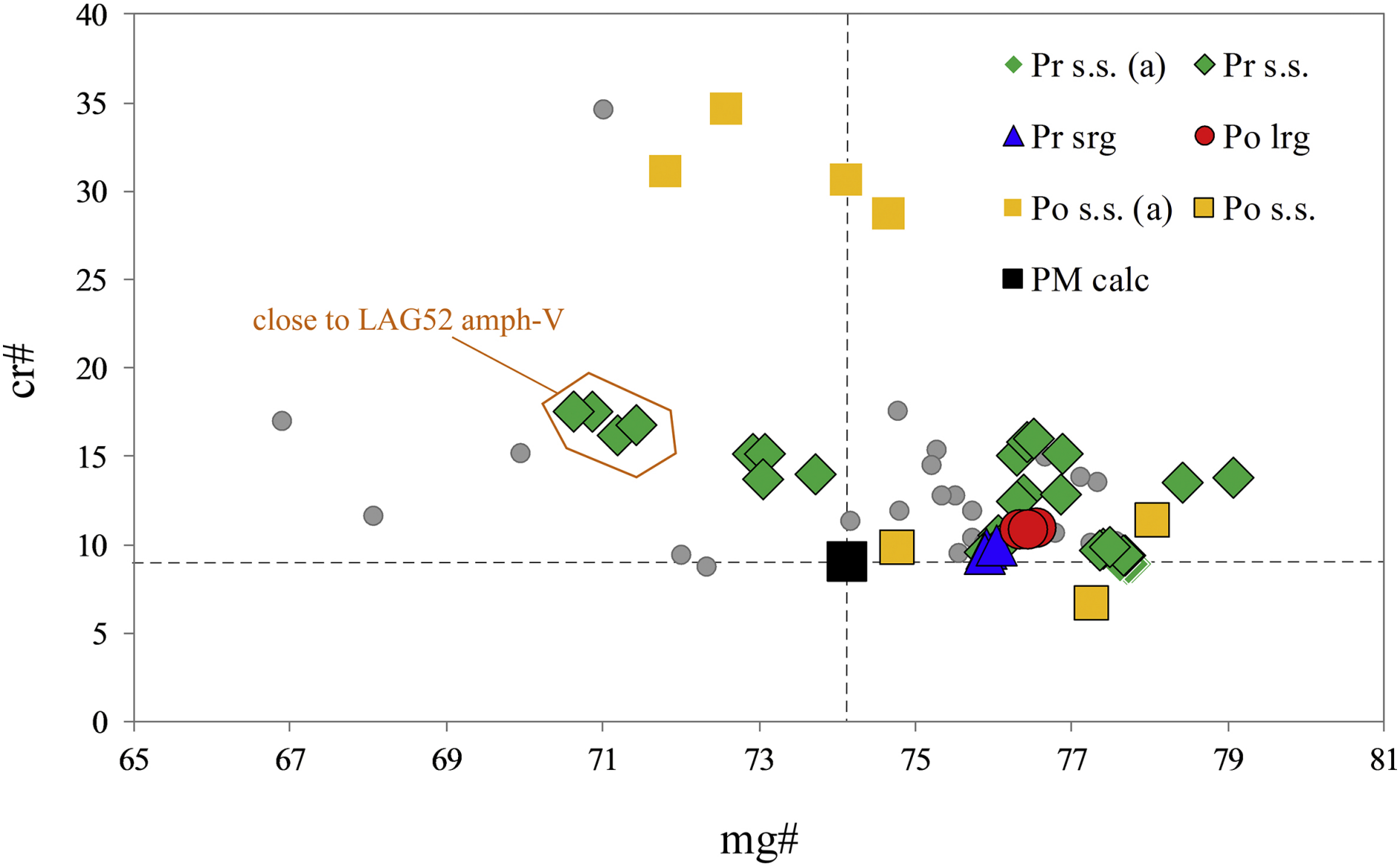
Pr s.s. (a)
Pr s.s.
Pr srg
Po lrg
Po s.s. (a)
Po s.s.
PM calc
close to LAG52 amph-V
cr#
mg#
0
5
10
15
20
25
30
35
40
65
67
69
71
73
75
77
79
81

Figure 5

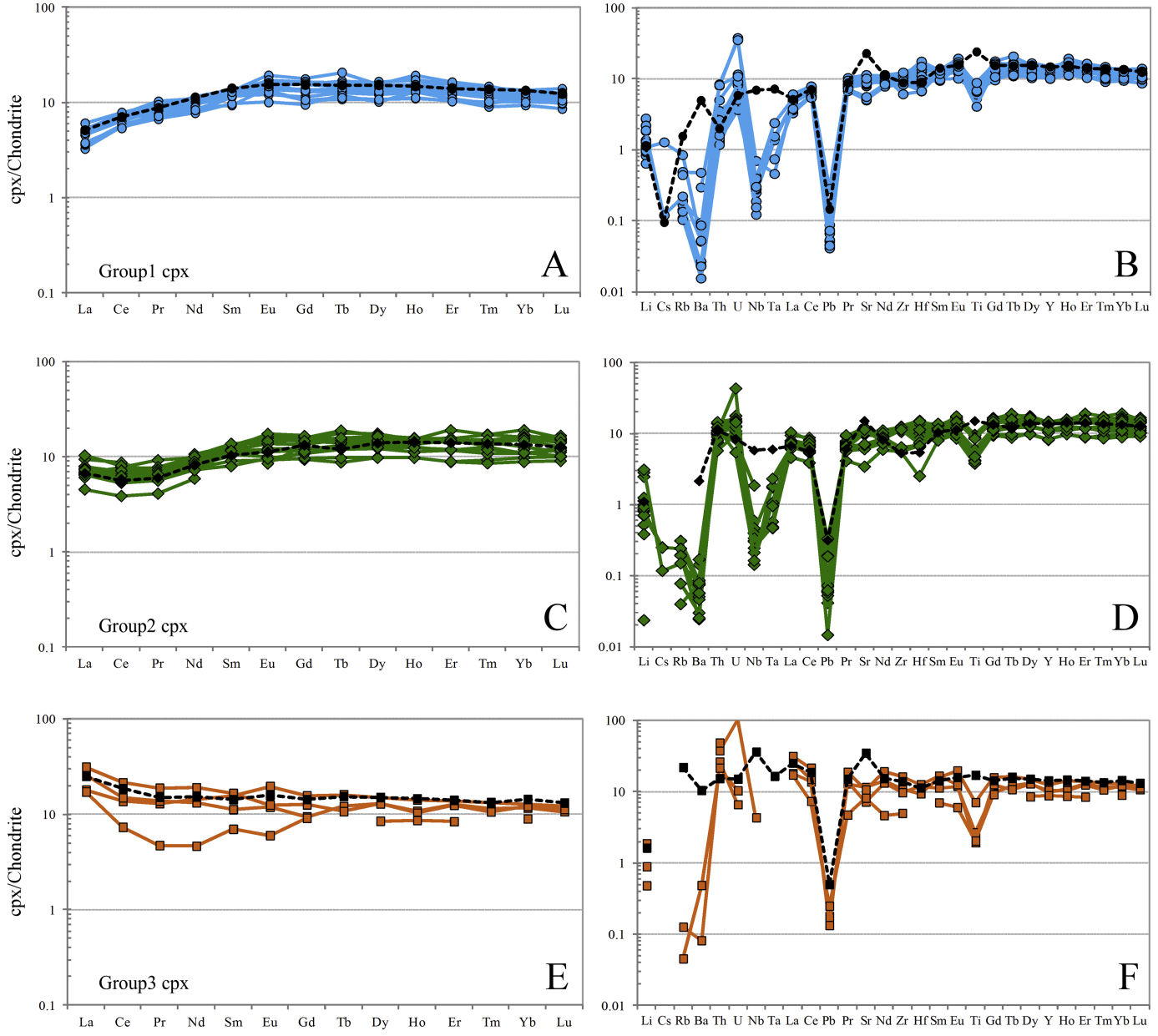
cpx/Chondrite
100
10
1
0.1
0.01
La Ce Pr Nd Sm Eu Gd Tb Dy Ho Er Tm Yb Lu
Li Cs Rb Ba Th U Nb Ta La Ce Pb Pr Sr Nd Zr Hf Sm Eu Ti Gd Tb Dy Y Ho Er Tm Yb Lu
Group1 cpx
A
B
Group2 cpx
C
D
Group3 cpx
E
F

Figure 6

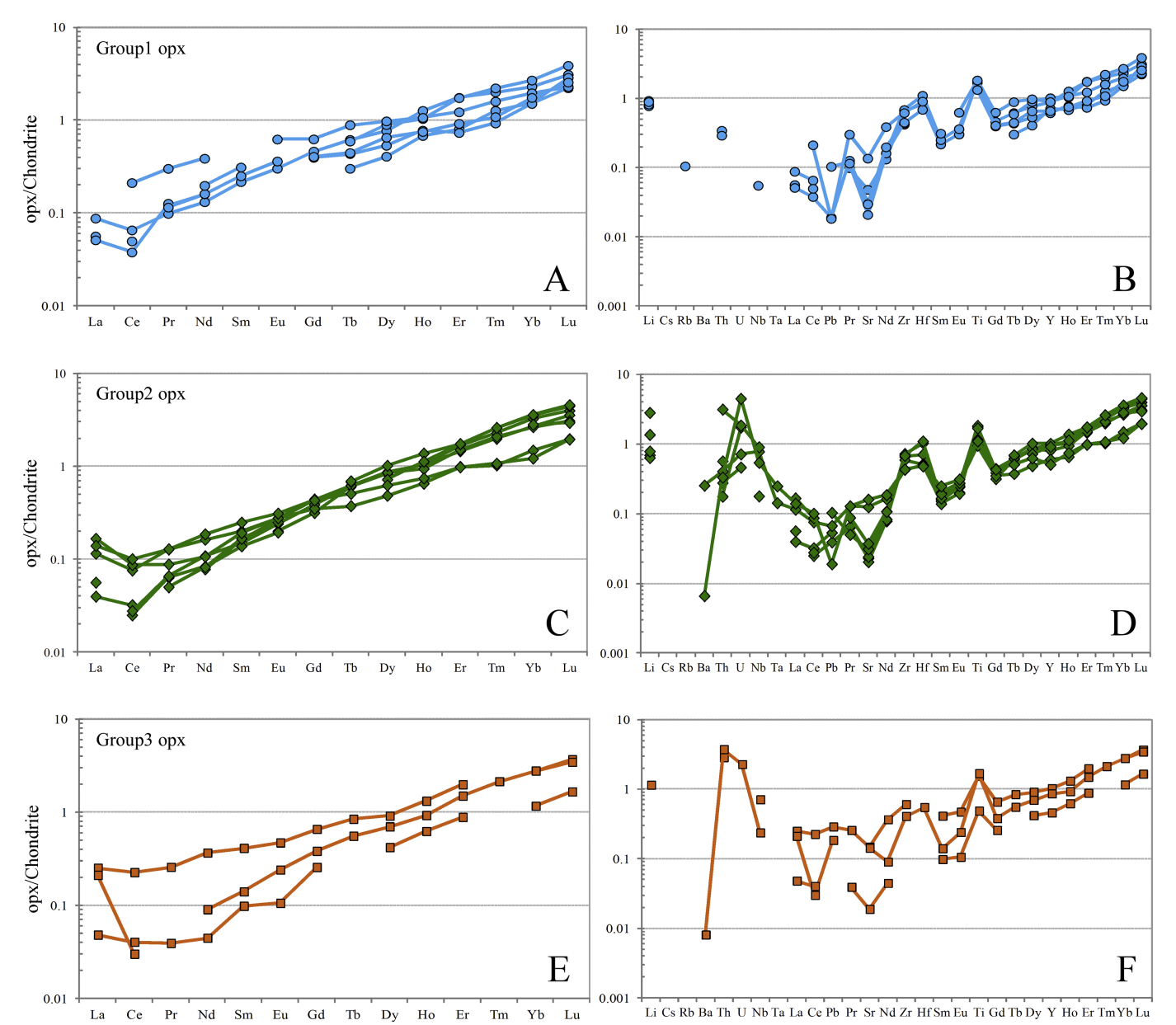
Group1 opx
opx/Chondrite
10
1
0.1
0.01
La Ce Pr Nd Sm Eu Gd Tb Dy Ho Er Tm Yb Lu
A
0.001
Li Cs Rb Ba Th U Nb Ta La Ce Pb Pr Sr Nd Zr Hf Sm Eu Ti Gd Tb Dy Y Ho Er Tm Yb Lu
B
Group2 opx
C
D
Group3 opx
E
F

Figure 7

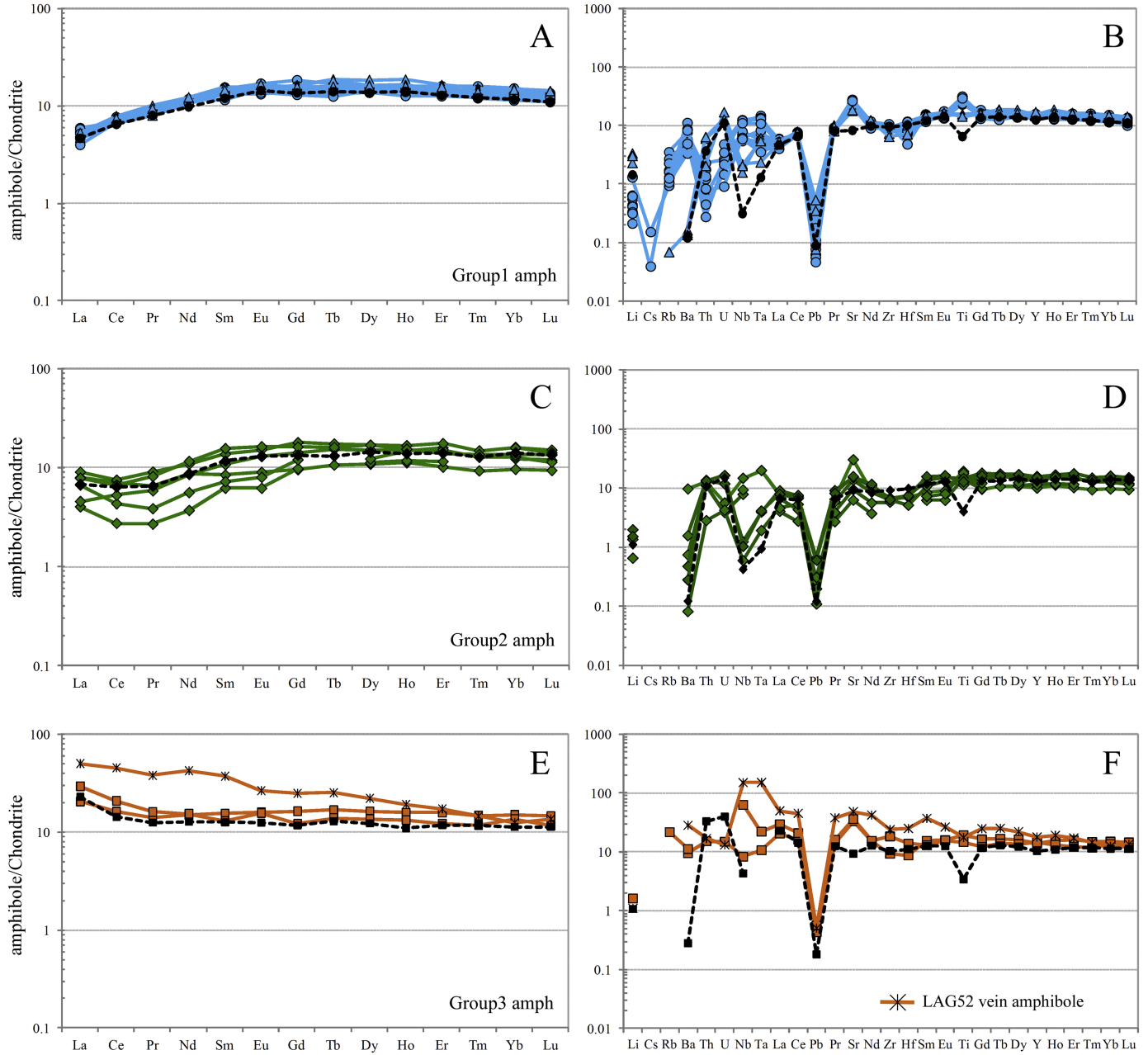
A
amphibole/Chondrite
Group1 amph
La Ce Pr Nd Sm Eu Gd Tb Dy Ho Er Tm Yb Lu
B
Li Cs Rb Ba Th U Nb Ta La Ce Pb Pr Sr Nd Zr Hf Sm Eu Ti Gd Tb Dy Y Ho Er Tm Yb Lu
C
Group2 amph
D
E
Group3 amph
F
LAG52 vein amphibole

Figure 8

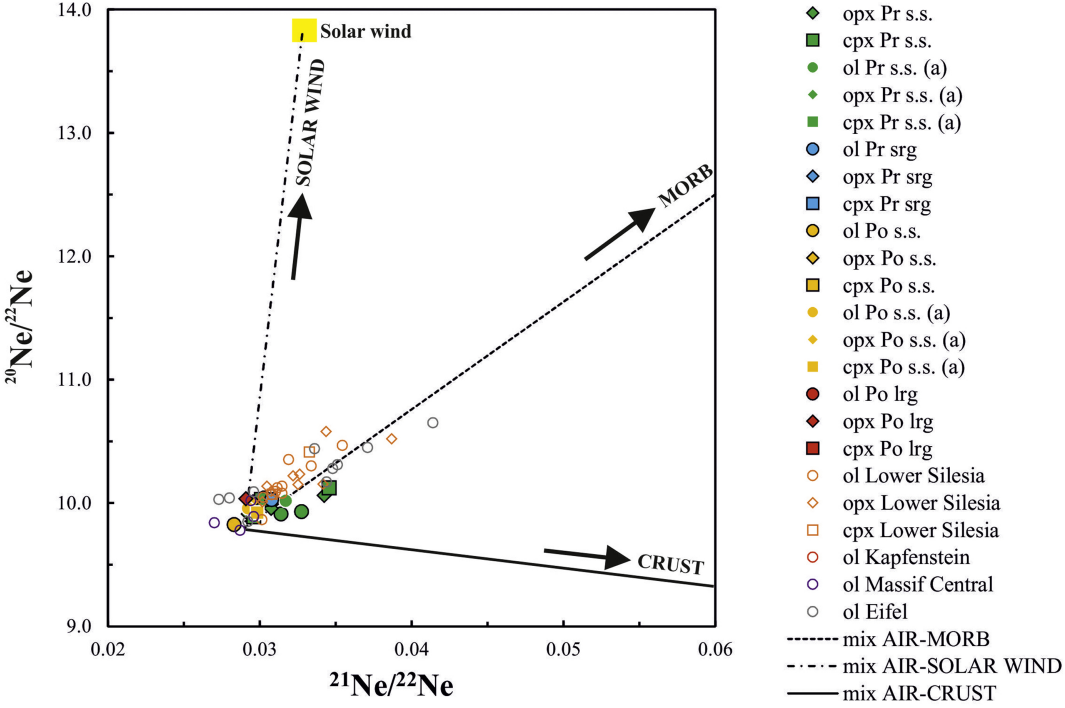
Solar wind
SOLAR WIND
MORB
CRUST
$^{20}Ne/^{22}Ne$
$^{21}Ne/^{22}Ne$
14.0
13.0
12.0
11.0
10.0
9.0
0.02
0.03
0.04
0.05
0.06
ol Pr s.s.
opx Pr s.s.
cpx Pr s.s.
ol Pr s.s. (a)
opx Pr s.s. (a)
cpx Pr s.s. (a)
ol Pr srg
opx Pr srg
cpx Pr srg
ol Po s.s.
opx Po s.s.
cpx Po s.s.
ol Po s.s. (a)
opx Po s.s. (a)
cpx Po s.s. (a)
ol Po lrg
opx Po lrg
cpx Po lrg
ol Lower Silesia
opx Lower Silesia
cpx Lower Silesia
ol Kapfenstein
ol Massif Central
ol Eifel
mix AIR-MORB
mix AIR-SOLAR WIND
mix AIR-CRUST

Figure 9

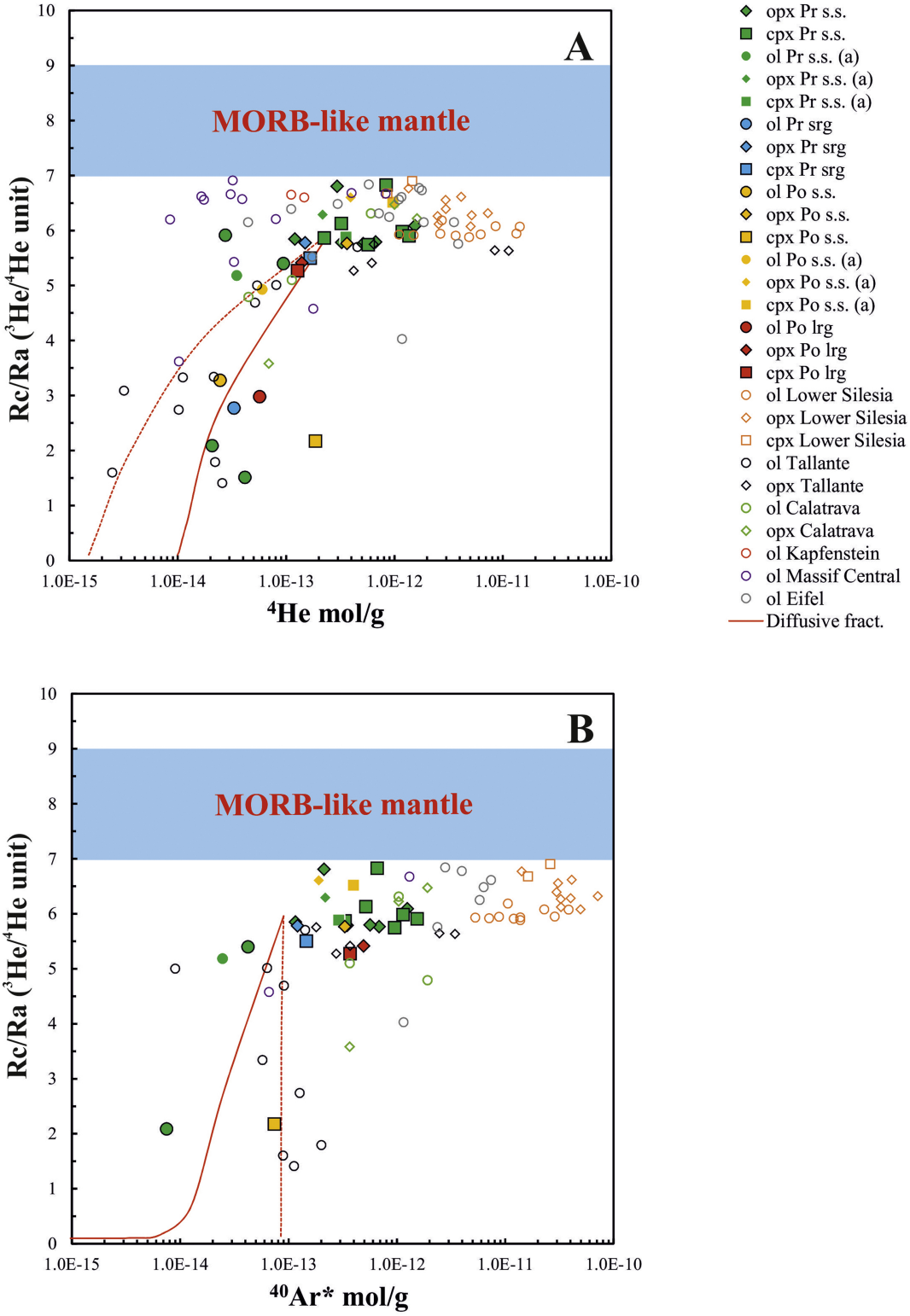
A
MORB-like mantle
Rc/Ra (^{3}He/^{4}He unit)
^{4}He mol/g
1.0E-15
1.0E-14
1.0E-13
1.0E-12
1.0E-11
1.0E-10
0
1
2
3
4
5
6
7
8
9
10
ol Pr s.s.
opx Pr s.s.
cpx Pr s.s.
ol Pr s.s. (a)
opx Pr s.s. (a)
cpx Pr s.s. (a)
ol Pr srg
opx Pr srg
cpx Pr srg
ol Po s.s.
opx Po s.s.
cpx Po s.s.
ol Po s.s. (a)
opx Po s.s. (a)
cpx Po s.s. (a)
ol Po lrg
opx Po lrg
cpx Po lrg
ol Lower Silesia
opx Lower Silesia
cpx Lower Silesia
ol Tallante
opx Tallante
ol Calatrava
opx Calatrava
ol Kapfenstein
ol Massif Central
ol Eifel
Diffusive fract.
B
MORB-like mantle
Rc/Ra (^{3}He/^{4}He unit)
^{40}Ar* mol/g
1.0E-15
1.0E-14
1.0E-13
1.0E-12
1.0E-11
1.0E-10
0
1
2
3
4
5
6
7
8
9
10

Figure 10

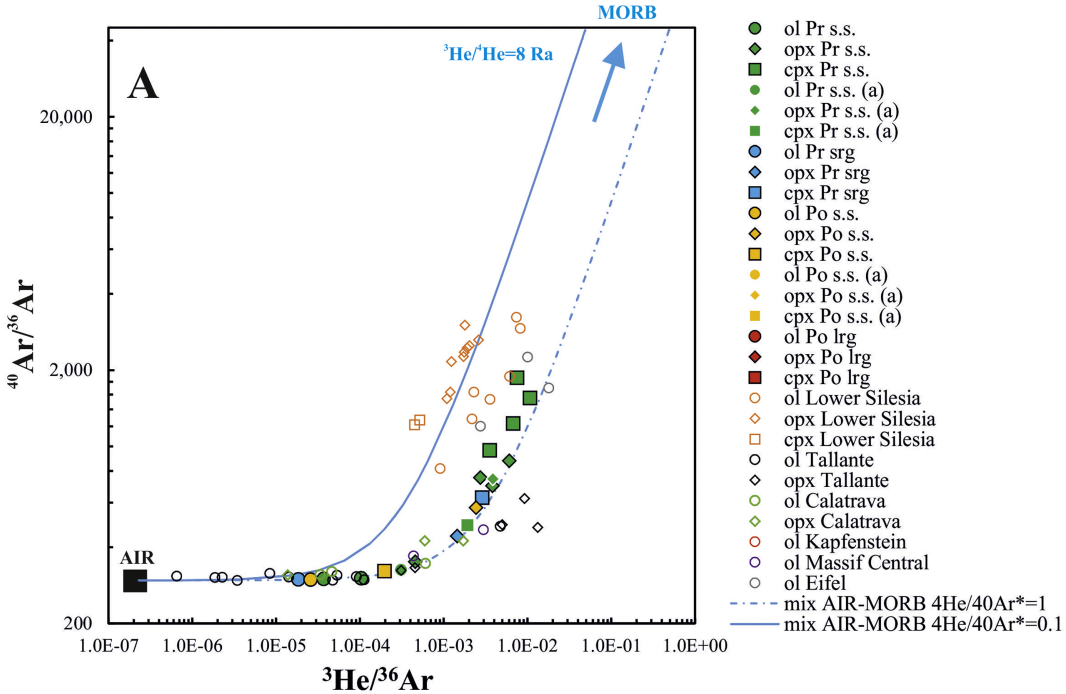
A
MORB
^{3}He/^{4}He=8 Ra
AIR
20,000
2,000
200
1.0E-07
1.0E-06
1.0E-05
1.0E-04
1.0E-03
1.0E-02
1.0E-01
1.0E+00
^{40}Ar/^{36}Ar
^{3}He/^{36}Ar
ol Pr s.s.
opx Pr s.s.
cpx Pr s.s.
ol Pr s.s. (a)
opx Pr s.s. (a)
cpx Pr s.s. (a)
ol Pr srg
opx Pr srg
cpx Pr srg
ol Po s.s.
opx Po s.s.
cpx Po s.s.
ol Po s.s. (a)
opx Po s.s. (a)
cpx Po s.s. (a)
ol Po lrg
opx Po lrg
cpx Po lrg
ol Lower Silesia
opx Lower Silesia
cpx Lower Silesia
ol Tallante
opx Tallante
ol Calatrava
opx Calatrava
ol Kapfenstein
ol Massif Central
ol Eifel
mix AIR-MORB 4He/40Ar*=1
mix AIR-MORB 4He/40Ar*=0.1

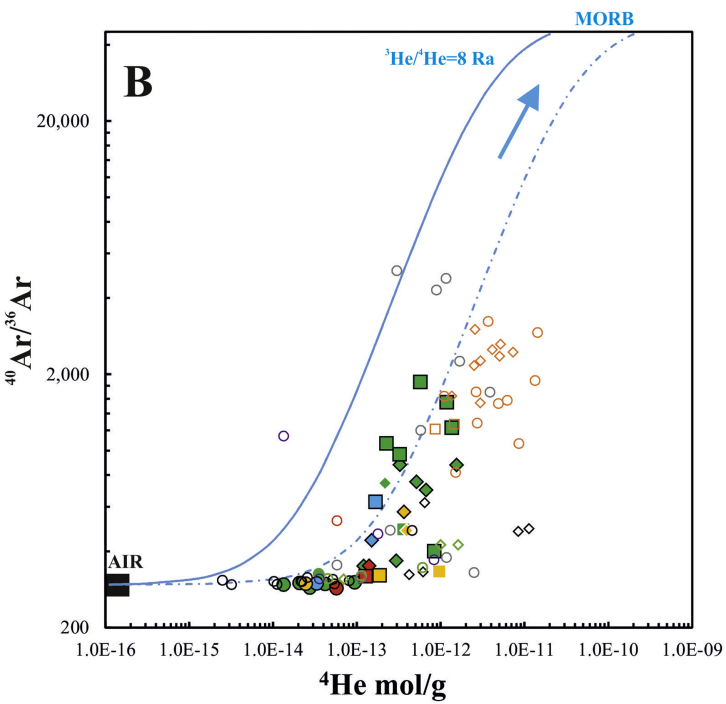
B
MORB
^{3}He/^{4}He=8 Ra
AIR
20,000
2,000
200
1.0E-16
1.0E-15
1.0E-14
1.0E-13
1.0E-12
1.0E-11
1.0E-10
1.0E-09
^{40}Ar/^{36}Ar
^{4}He mol/g

Figure 11

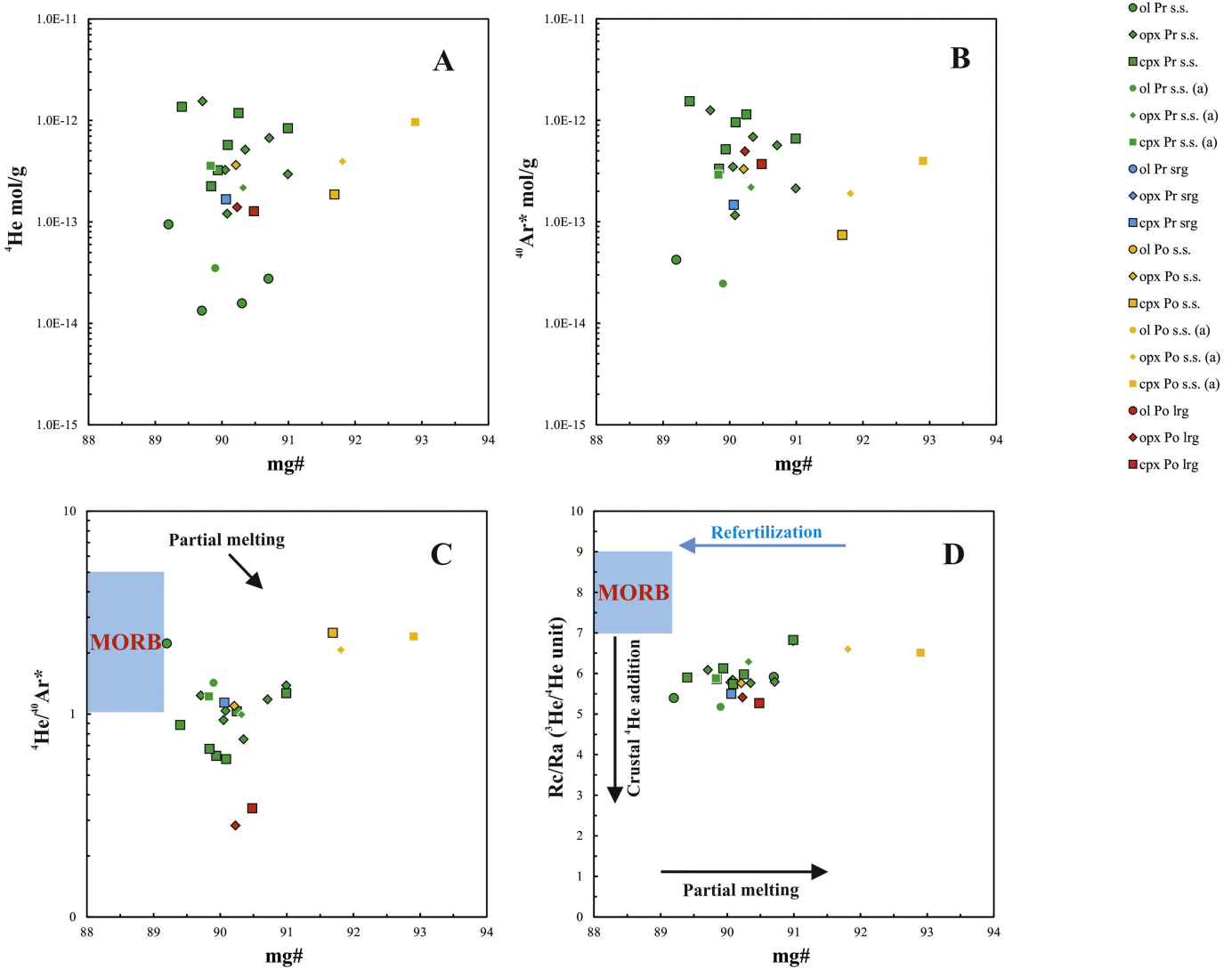
A
B
C
D
^{4}He mol/g
^{40}Ar* mol/g
^{4}He/^{40}Ar*
Rc/Ra (^{3}He/^{4}He unit)
mg#
1.0E-11
1.0E-12
1.0E-13
1.0E-14
1.0E-15
88
89
90
91
92
93
94
0
1
2
3
4
5
6
7
8
9
10
Partial melting
MORB
Refertilization
Crustal ^{4}He addition
ol Pr s.s.
opx Pr s.s.
cpx Pr s.s.
ol Pr s.s. (a)
opx Pr s.s. (a)
cpx Pr s.s. (a)
ol Pr srg
opx Pr srg
cpx Pr srg
ol Po s.s.
opx Po s.s.
cpx Po s.s.
ol Po s.s. (a)
opx Po s.s. (a)
cpx Po s.s. (a)
ol Po lrg
opx Po lrg
cpx Po lrg

Figure 12

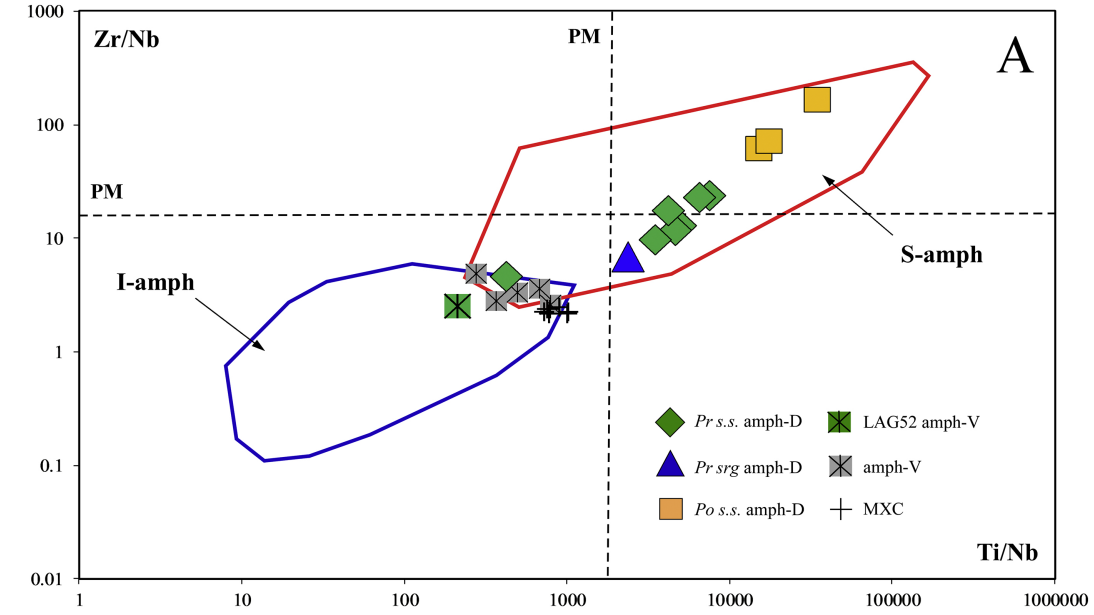
Zr/Nb
PM
A
PM
S-amph
I-amph
Pr s.s. amph-D
LAG52 amph-V
Pr srg amph-D
amph-V
Po s.s. amph-D
MXC
Ti/Nb
1000
100
10
1
0.1
0.01
1
10
100
1000
10000
100000
1000000

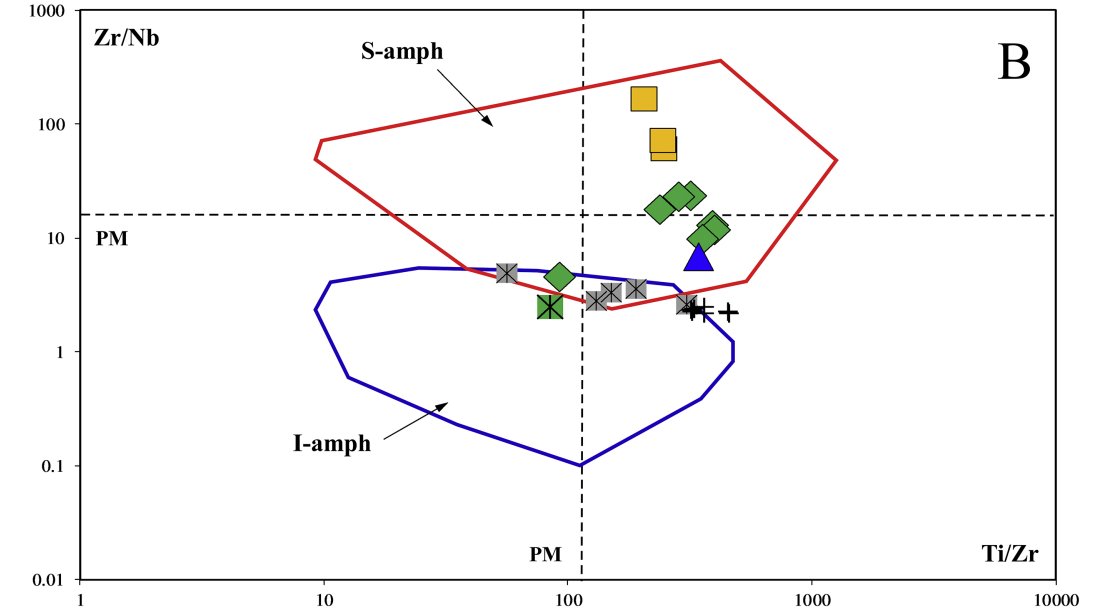
Zr/Nb
S-amph
B
PM
I-amph
PM
Ti/Zr
1000
100
10
1
0.1
0.01
1
10
100
1000
10000

Figure 13

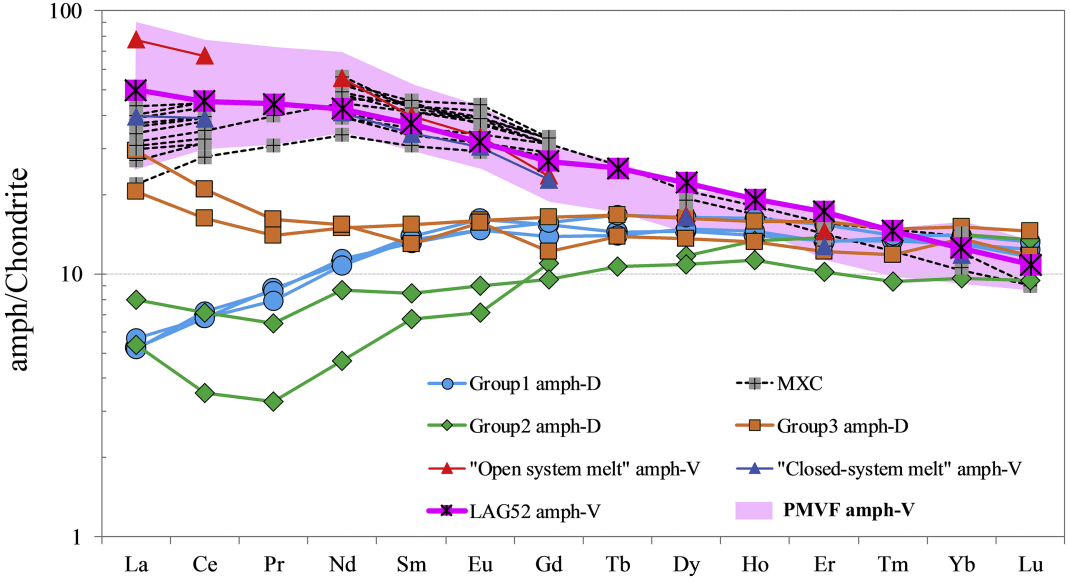
100
10
1
amph/Chondrite
La
Ce
Pr
Nd
Sm
Eu
Gd
Tb
Dy
Ho
Er
Tm
Yb
Lu
Group1 amph-D
MXC
Group2 amph-D
Group3 amph-D
"Open system melt" amph-V
"Closed-system melt" amph-V
LAG52 amph-V
PMVF amph-V

Figure 14

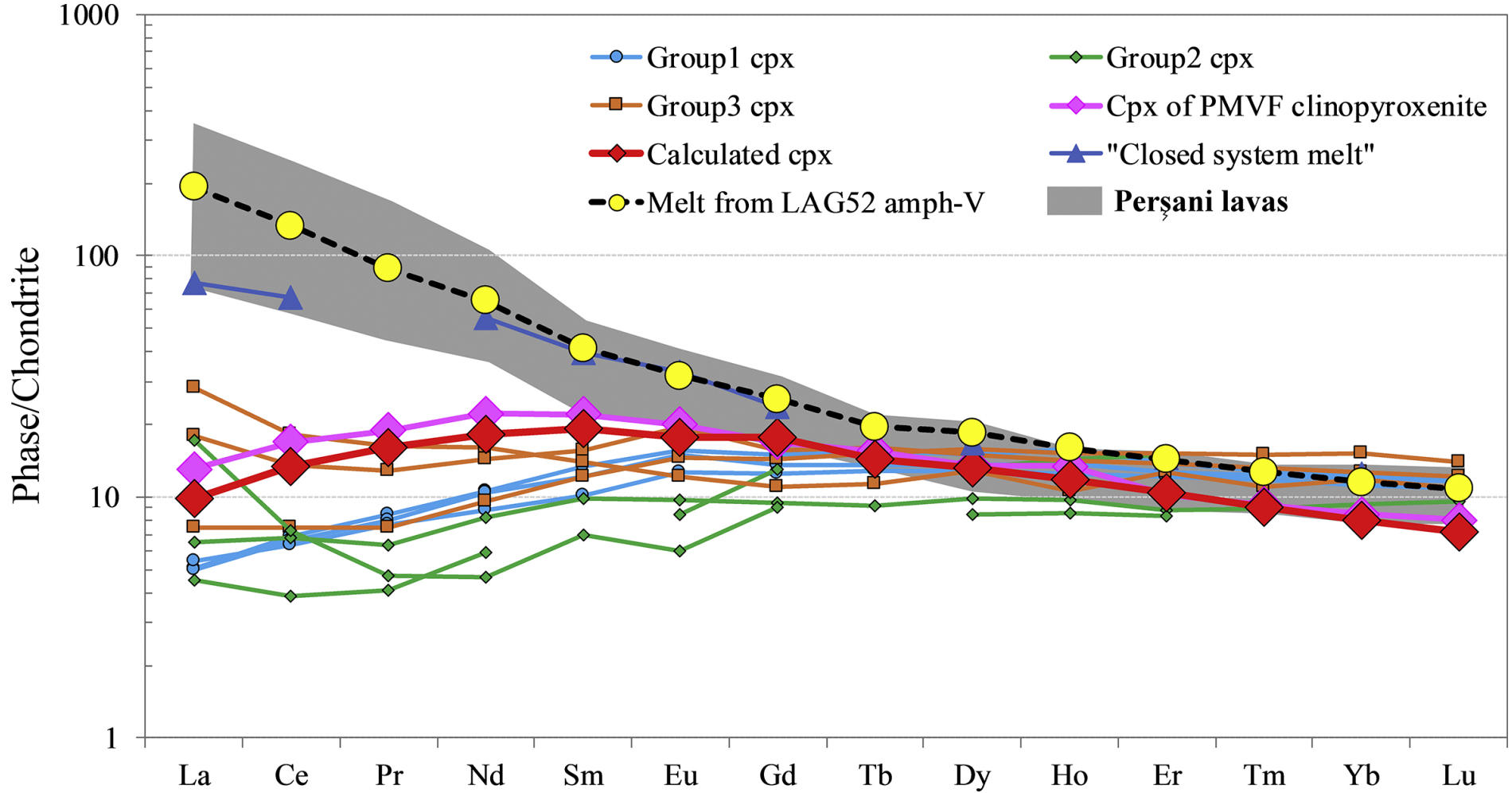
1000
100
10
1
Phase/Chondrite
Group1 cpx
Group2 cpx
Group3 cpx
Cpx of PMVF clinopyroxenite
Calculated cpx
"Closed system melt"
Melt from LAG52 amph-V
Perşani lavas
La
Ce
Pr
Nd
Sm
Eu
Gd
Tb
Dy
Ho
Er
Tm
Yb
Lu

Figure 15